THE DEPARTMENT OF ONCOLOGY-PATHOLOGY
Karolinska Institutet, Stockholm, Sweden

RADIATION DOSE AND X-RAY BEAM MODELLING IN DIAGNOSTIC AND INTERVENTIONAL RADIOLOGY USING MONTE CARLO METHODS

Artur Omar

Karolinska Institutet

Stockholm 2020

Cover Image:
Monte Carlo simulated electron tracks in a tungsten target representing a typical x-ray tube anode. The PENELOPE code *shower* was used to simulate 50 electrons incident upon a $10\,\mu\mathrm{m}$ thick tungsten slab with an initial kinetic energy of 100 keV; the colour (i.e., the red hue) of the track is proportional to the kinetic energy (red to pink).

Published by Karolinska Institutet
Printed by US-AB 2020

ISBN 978-91-8016-009-4

RADIATION DOSE AND X-RAY BEAM MODELLING IN DIAGNOSTIC AND INTERVENTIONAL RADIOLOGY USING MONTE CARLO METHODS
THESIS FOR DOCTORAL DEGREE (Ph.D.)

By

Artur Omar

Principal supervisor	Doctor Gavin Poludniowski, Karolinska Institutet
Co-supervisors	Professor Pedro Andreo, Karolinska Institutet
	Docent Annette Fransson, Karolinska Institutet
Opponent	Professor Guillaume Landry, Ludwig-Maximilians-Universität München
Examination Board	Docent Anja Almén, Lunds Universitet
	Professor Magnus Båth, Göteborgs Universitet
	Docent Massimiliano Colarieti-Tosti, Kungliga Tekniska Högskolan

Contents

Abstract

Although medical imaging is essential for the diagnosis and treatment of a wide range of medical conditions, the radiation dose from x-ray examinations is one of the largest contributors to the exposure of the world's population. It is therefore the responsibility of healthcare professionals to ensure that examinations are justified (a net benefit) and optimized (as low dose as reasonably achievable). In order to better understand the risks associated with medical exposures, methods for systematic and accurate patient dose estimation are necessary. This is addressed in the present thesis by introducing improved methods for x-ray beam and radiation dose modelling in diagnostic and interventional radiology. The thesis is comprised of two interconnected parts, summarized as follows.

The first part of the thesis describes the development of a deterministic model for the energy and angular distribution of x rays emitted from an x-ray tube. The model combines Monte Carlo-calculated results and theoretical physics data to account for the depth, energy, and angular distribution of bremsstrahlung and characteristic x rays produced in an x-ray tube anode. The model is an improvement over previous models, especially for low kilovoltage x-ray beams (below 50 kV), and it is reliable for a broader angular distribution of the x-ray emission, making it suitable for the prediction of central-axis spectra, as well as off-axis effects such as the (anode) heel effect. It is able to reproduce narrow-beam Monte Carlo calculations to within 0.5% in terms of the aluminum half-value layer thickness (HVL), and is in good agreement ($< 2\%$ in HVL) with measured spectra for typical diagnostic and therapeutic x-ray beams.

The second part concerns the development and application of a framework for systematic estimation of patient organ absorbed doses. The framework includes a method for reconstructing the exposure geometry based on non-proprietary access to widely available radiation dose structured reports (RDSR). By combining the framework with an x-ray source model (such as the one developed in this work), and Monte Carlo simulations of radiation transport, systematic estimation of patient doses is possible, something that has traditionally been difficult to achieve. A prototype implementation of the framework is demonstrated for selected radiation dose estimations. The applications are shown to provide an enhanced understanding of the patient radiation exposure and the risks associated with radiation, which is useful for the optimization of clinical methods and protocols.

The methods developed in this work can be used by healthcare professionals as well as researchers to justify and optimize each medical x-ray exposure performed in the treatment of a patient, thereby ensuring the safe use of radiation in medicine.

List of papers

The doctoral thesis is based on the following papers, which are referred to in the text by their Roman numerals:

I Omar A, Bujila R, Fransson A, Andreo P and Poludniowski G 2016 A framework for organ dose estimation in x-ray angiography and interventional radiology based on dose-related data in DICOM structured reports *Phys. Med. Biol.* **61** 3063–3083

II Omar A, Andreo P and Poludniowski G 2018 Performance of different theories for the angular distribution of bremsstrahlung produced by keV electrons incident upon a target *Radiat. Phys. Chem.* **148** 73–85

III Omar A, Andreo P and Poludniowski G 2018 A model for the emission of K and L x rays from an x-ray tube *Nucl. Instrum. Methods Phys. Res. B* **437** 36–47

IV Karambatsakidou A, Omar A, Fransson A and Poludniowski G 2019 Calculating organ and effective doses in paediatric interventional cardiac radiology based on DICOM structured reports — Is detailed examination data critical to dose estimates? *Phys. Medica* **57** 17–24

V Omar A, Andreo P and Poludniowski G 2020 A model for the energy and angular distribution of x rays emitted from an x-ray tube. Part I. Bremsstrahlung production *Med. Phys.* **47**(10) 4763–4774

VI Omar A, Andreo P and Poludniowski G 2020 A model for the energy and angular distribution of x rays emitted from an x-ray tube. Part II. Validation of x-ray spectra from 20 to 300 kV *Med. Phys.* **47**(9) 4005–4019

Related publications not included in the thesis:

i Omar A, Benmakhlouf H, Marteinsdottir M, Bujila R, Nowik P and Andreo P 2014 Monte Carlo investigation of backscatter factors for skin dose determination in interventional neuroradiology procedures *in* 'Physics of Medical Imaging' **Vol 9033** (Bellingham: International Society for Optics and Photonics)

ii Karambatsakidou A, Omar A, Chehrazi B, Rück A, Scherp J and Fransson A 2016 Skin dose, effective dose and related risk in transcatheter aortic valve implantation (TAVI) procedures: is the cancer risk acceptable for younger patients *Radiat. Prot. Dosim.* **169** 225–231

iii Edström E, Burström G, Omar A, Nachabe R, Söderman M, Persson O, Gerdhem P and Elmi-Terander A 2020 Augmented reality surgical navigation in spine surgery to minimize staff radiation exposure *Spine* **45** E45-E53

iv Bujila R, Omar A and Poludniowski G 2020 A validation of SpekPy: a software toolkit for modelling x-ray tube spectra *Phys. Medica* **75** 44–54

v Omar A 2020 Reconstructing the exposure geometry in x-ray angiography and interventional radiology *in* 'Diagnostic Radiology Physics with MATLAB: a problem solving approach' edited by Helmenkamp J, Bujila R and Poludniowski G (CRC Press, Boca Raton, FL).

List of acronyms

AAPM	The American Association of Physicists in Medicine
ALARA	As Low As Reasonably Achievable
CBCT	Cone-Beam Computed Tomography
CPE	Charged Particle Equilibrium
CSDA	Continuous Slowing Down Approximation
CT	Computed Tomography
DCS	Differential Cross Section
DICOM	Digital Imaging and Communications in Medicine
EADL	Evaluated Atomic Data Library
EPDL	Evaluated Photon Data Library
HVL	Half-Value Layer thickness
IAEA	International Atomic Energy Agency
ICRP	International Commission on Radiological Protection
ICRU	International Commission on Radiation Units and Measurements
IGT	Image-Guided Therapy
IMDR	Intensity Modulated Diagnostic Radiology
IPEM	Institute of Physics and Engineering in Medicine
MC	Monte Carlo
MRI	Magnetic Resonance Imaging
NEMA	National Electrical Manufacturers Association
NIST	National Institute of Standards and Technology
NURBS	Non-Uniform Rational B-Spline
PTB	Physikalisch-Technische Bundesanstalt
RBE	Relative Biological Effectiveness
RBM	Red Bone Marrow
RDSR	Radiation Dose Structured Report
UNSCEAR	United Nations Scientific Committee on the Effects of Atomic Radiation

Chapter 1

Introduction

Although the use of x rays for non-invasive imaging has led to vast improvements in the diagnosis and treatment of medical conditions, the associated radiation exposure has become a major contributor to the exposure of the world's population (UNSCEAR, 2008). The number of radiological examinations performed annually has seen a steady increase over the last few decades as x-ray imaging technologies have become more efficient and accurate. According to the latest global survey reported by the United Nations Scientific Committee on the Effects of Atomic Radiation (UNSCEAR), 490 x-ray examinations per 1000 individuals were performed annually between 1997 and 2007, which was an increase of 50% from the the former survey in 1991–1996. For comparison, in Europe the annual frequency between 2007–2010 was 1100 examinations per 1000 individuals (770 per 1000 in Sweden) according to the European Commission (2015). Some types of radiological examinations, such as interventional x-ray angiography procedures, may expose patients to absorbed doses of ionizing radiation that can induce tissue reactions in addition to stochastic effects (e.g., cancer) (ICRP, 2012). The number of such procedures performed annually has also been on the rise due to rapid advances in minimally invasive techniques, a trend that is expected to continue (Kagadis *et al.*, 2012).

In order to ensure that radiation is used as safely as possible, the International Commission on Radiological Protection (ICRP) has formulated the *fundamental principles of radiological protection* (ICRP, 2007*b*):

Justification	"Any decision that alters the radiation exposure situation should do more good than harm"
Optimization	"Doses should all be kept as low as reasonably achievable" (ALARA)
Dose limitation	"The total dose to any individual [...] should not exceed the appropriate limits"

With these principles in mind, several international organizations issued a joint position statement in 2012, emphasizing the importance of systematic recording, reporting, and tracking of patients' exposures (IAEA, 2012). They also identified several obstacles, including challenges associated with dose and risk assessment. One of the main issues being how to translate a medical exposure to a patient dose (NRC, 2012).

X-ray imaging systems display a measured or calculated dose index that indicates the amount of radiation delivered per radiological examination. Such measurements, however, do not necessarily reflect the patient's absorbed dose, as the patient (size, morphology, and anatomic region) is not considered. Moreover, different imaging modalities (e.g., computed tomography and radiography) display different dose indices that can not be directly combined to estimate the total exposure history of an individual patient or patient population. Hence, in order to compare the radiation exposure for different imaging modalities and to relate it to a meaningful measure of risk, the absorbed dose to organs has to be considered. This represents a challenge in itself, however, as both patient- and x-ray source-related factors have to be accounted for in order to achieve the recommended accuracy in the dosimetry (ICRU, 2005).

The recommended accuracy for patient dosimetry depends on the dose level and the potential risk. The American Association of Physicists in Medicine (AAPM TG-6; Wagner *et al.*, 1992) and the International Atomic Energy Agency (IAEA TRS-457; Alm-Carlsson *et al.*, 2007) have both recommend an accuracy of 20% (95% confidence limits, $k = 2$) in dosimetry measurements when used for estimating the absolute risk of a stochastic effect. The rationale was that since the uncertainty in the absolute risk for a stochastic effect is high for the relatively low doses delivered, an accuracy of 20% is sufficient. A higher accuracy of 7% ($k = 2$), which is similar to the accuracy of dosimetry measurements in radiotherapy, is recommended when tissue reactions are expected or for estimating the exposure of paediatric patient (ICRP, 2007*a*). Although the quoted figures relate to the accuracy of directly measured dosimetry quantities, they indicate a general level of accuracy that should be pursued in patient dosimetry.

This thesis aims to address some of the challenges associated with patient dose assessment in diagnostic and interventional radiology, by providing improved methods for radiation dose and x-ray beam modelling. Interventional radiology is of particular interest as the the doses delivered can be substantial, which warrants a higher accuracy in the dosimetry. Some background on the main topics of this thesis is provided in the next chapter (Chapter 2), along with background on the principal methodology used, the Monte Carlo (MC) method. The methods and results produced in this work are presented in the subsequent chapters. Chapter 3 outlines the framework for dose estimation developed in this thesis, which incorporates both patient- and x-ray source-related factors; the x-ray source model is described in Chapter 4. In Chapter 5, the practical use of the methods developed is demonstrated for various dose estimations.

1.1 Research aims

The papers included in this thesis address the following research aims:

- To develop a framework for patient dose estimation that considers in detail the physical context of each individual exposure (using an x-ray source model), and to estimate organ absorbed and effective doses for interventional radiology procedures (Paper I & IV).
  - *Can DICOM radiation dose structured reports (RDSR) be used for more accurate patient dose estimations?*
- To develop an improved model for bremsstrahlung emission from an x-ray tube by considering in greater detail the electron and intrinsic bremsstrahlung angular distributions (Paper II & V).
  - *Can a more accurate model for the energy and angular distribution of bremsstrahlung be developed?*
- To develop an improved model for the emission of K and L x rays from an x-ray tube, considering the depth distribution of x-ray fluorescence (Paper III).
  - *Can a more accurate model for the prediction of the number of characteristic x-rays emitted in a given direction be developed?*
- To present and validate an x-ray source model (bremsstrahlung and characteristic x rays) for the energy range 20–300 kV (Paper VI).
  - *Is the model developed in this work an improvement over previous models in terms of predictions of the x-ray energy absorption and the angular distribution of the x-ray emission?*

Chapter 2

Background

2.1 Radiation dose modelling

The patient radiation exposure can be assessed by determining the absorbed dose to internal organs (and the related quantity of effective dose), as well as determining the entrance surface dose. The latter is especially relevant when the dose delivered to the skin may induce tissue reactions. The following sections provide some background on these two aspects of patient dosimetry.

2.1.1 Organ absorbed dose and effective dose

Accurate estimation of organ doses has traditionally been a challenge. The most accurate methods have consisted of clinical measurements on patients to determine the dose delivered to superficial organs, like the skin, the thyroid gland, and the lens of the eye (Vano *et al.*, 2001; Theodorakou and Horrocks, 2003). Such approaches are, however, not suited for systematic dose estimation considering the large number of x-ray examinations performed on a daily basis in a hospital. Instead, alternative computational methods have been developed that make use of examination-specific conversion coefficients that relate organ absorbed doses to readily measurable quantities, such as incident air kerma, air kerma-area product (P_{KA}), or computed tomography (CT) kerma index (C_{K}). These quantities are typically displayed by x-ray imaging systems, and can be measured under reference conditions (or non-reference conditions with appropriate corrections) using an ionization chamber calibrated at a standards laboratory in terms of air kerma free-in-air. The air kerma based dosimetry is well-established in diagnostic radiology according to the IAEA TRS-457 code of practice (Alm-Carlsson *et al.*, 2007) and the International Commission on Radiation Units and Measurements (ICRU) report 74 (ICRU, 2005).

For diagnostic x-ray energies the absorbed dose can generally be approximated by kerma (kinetic energy released per unit mass), as the electrons released in photon interactions have short ranges and thus deposit their entire kinetic energy locally — within 0.3 mm in soft tissue according to the continuous slowing down approximation (CSDA) (Berger *et al.*, 2005). Kerma and collision kerma for a fluence Φ of photons of energy k can be expressed as (ICRU, 2011),

$$\begin{aligned} K &= k\,\Phi\,\mu_{\mathrm{tr}}/\rho \\ K_{\mathrm{col}} &= k\,\Phi\,\mu_{\mathrm{en}}/\rho = K(1-g), \end{aligned} \tag{2.1}$$

where μ_{tr}/ρ and μ_{en}/ρ are, respectively, the mass energy transfer and the mass energy absorption coefficients in a given medium, and g is the fraction of the energy lost by the photon-generated electrons in radiative processes. Note that radiative energy losses are practically negligible ($g \approx 0$) for the energies and media relevant for diagnostic radiology dosimetry, making the kerma numerically equivalent to the collision kerma. Hence, the absorbed dose to a tissue (or organ) T can be determined as,

$$D_{\mathrm{T}} \equiv K_{\mathrm{T}} = \int \mathrm{d}k\; k\,\Phi_k\,[\mu_{\mathrm{en}}(k)/\rho]_{\mathrm{T}}, \tag{2.2}$$

where Φ_k is the photon fluence spectrum, i.e., the fluence differential in photon energy, and $[\mu_{\mathrm{en}}(k)/\rho]_{\mathrm{T}}$ is the mass energy-absorption coefficient for photons of energy k in tissue T.

Organ doses can thus be estimated using eq. (2.2), with the photon fluence spectrum determined, for instance, by simulating the photon transport in tissue using the Monte Carlo method. An important exception is the absorbed dose to red bone marrow (RBM), which is located in small cavities in trabecular bone. The cavities are too small for charged particle equilibrium (CPE) to be established, resulting in the absorbed dose being higher than that predicted by kerma due to an influx of electrons released by photoelectric absorption (and Compton scattering) in the surrounding trabecular bone matrix (King and Spiers, 1985). This can be accounted for by using a photon energy dependent kerma-to-dose conversion factor (or dose enhancement factor), which increases the estimated active bone marrow dose by a percentage that depends on which skeletal bone has been irradiated (Lee *et al.*, 2006).

As a complement to organ absorbed dose, the International Commission on Radiological Protection (ICRP, 1991) recommends the use of *effective dose* as a protection quantity that expresses a non-uniform exposure in terms of an equivalent whole-body exposure (ICRP, 1996). The effective dose is a quantity that can not be directly measured, but is instead assessed based on the organ absorbed dose in tissue T and radiation type R,

$$E = \sum_{\mathrm{T}} w_{\mathrm{T}} \sum_{\mathrm{R}} w_{\mathrm{R}}\, D_{\mathrm{T,R}}, \tag{2.3}$$

where the tissue weighting factor w_{T} represents the contribution of tissue (or organ) T to the total health detriment from stochastic effects (normalized so that $\sum_{\mathrm{T}} w_{\mathrm{T}} = 1$), and the radiation weighting factor w_{R} represents the relative biological effectiveness (RBE) of radiation type R (e.g., photons, electrons, and protons) with respect to stochastic effects. Note that the product of the radiation weighting factor and the organ dose corresponds to the radiation protection quantity of *equivalent dose*,

$$H_{\mathrm{T}} = \sum_{\mathrm{R}} w_{\mathrm{R}}\, D_{\mathrm{T,R}}. \tag{2.4}$$

It is emphasized that for photons the currently recommended value for the radiation weighting factor is one, making the equivalent dose (units of sievert) numerically identical to the organ absorbed dose (units of gray). Both the tissue and radiation weighting factors are subject to change with enhanced understanding of the biology and physics of radiation exposure. The currently recommended values for the weighting factors are provided in ICRP Publication 103 (ICRP, 2007*b*).

2.1.2 Entrance surface dose

The absorbed dose at the patient entrance surface, i.e., the skin, is of particular interest for x-ray examinations that deliver doses that may cause radiation induced tissue reactions. The x-ray examinations of main concern have traditionally been complex interventional radiology procedures, for which tissue reactions such as mild (> 2 Gy) to severe (> 6 Gy) skin injuries, and hair loss (> 3 Gy) (Balter *et al.*, 2010), have been observed. In order to assess the risk of developing a skin injury and to evaluate the need for early treatment, the absorbed dose to the patient's skin should be determined as accurately as possible. Recall that the IAEA TRS-457 code of practice states that a higher accuracy is needed in the dosimetry when tissue reactions are expected, recommending an accuracy of 7% ($k = 2$).

The entrance surface dose (or kerma) can be determined using the formalism outlined by Benmakhlouf *et al.* (2011), which parallels the in-air methodology described by Andreo and Nahum, (2007) for low-energy kilovoltage radiotherapy, and is consistent with ICRU-74 and IAEA TRS-457. The formalism describes the transfer of incident air kerma, $(K_{\mathrm{air}})_{\mathrm{air}}$, to the entrance surface water kerma, $(K_{\mathrm{w}})_{\mathrm{w}}$. Note that water is used in place of tissue for reasons of standardization of the medium, and to enable a parallelism with established methods for kilovoltage radiotherapy dosimetry (cf. Ma *et al.*, 2001). The formalism can be expressed as,

$$D_{\mathrm{w}} \equiv (K_{\mathrm{w}})_{\mathrm{w}} = (K_{\mathrm{air}})_{\mathrm{air}}\, B_{\mathrm{air}}\, [\mu_{\mathrm{en}}/\rho]^{\mathrm{p+s}}_{\mathrm{w,air}}\,, \tag{2.5}$$

where the backscatter factor, B_{air}, accounts for the dose contribution from photons backscattered to the entrance (water) surface, and the ratio of mass energy–absorption

coefficients, $[\mu_{\rm en}/\rho]^{\rm p+s}_{\rm w,air}$, converts air kerma into water kerma at the entrance surface (p+s indicates primary and scattered photons). The backscatter factor and the mass energy–absorption coefficient ratio are defined as,

$$B_{\rm air} = \frac{(K_{\rm air})^{\rm p+s}_{\rm w\text{-}surface}}{(K_{\rm air})_{\rm air}} = \frac{\int {\rm d}k\; k[\Phi_k]^{\rm p+s}_{\rm w\text{-}surface}\,[\mu_{\rm en}(k)/\rho]_{\rm air}}{\int {\rm d}k\; k[\Phi_k]^{\rm p}_{\rm air}\,[\mu_{\rm en}(k)/\rho]_{\rm air}}, \tag{2.6}$$

$$[\mu_{\rm en}/\rho]^{\rm p+s}_{\rm w,air} = \frac{(K_{\rm w})^{\rm p+s}_{\rm w\text{-}surface}}{(K_{\rm air})^{\rm p+s}_{\rm w\text{-}surface}} = \frac{\int {\rm d}k\; k[\Phi_k]^{\rm p+s}_{\rm w\text{-}surface}\,[\mu_{\rm en}(k)/\rho]_{\rm w}}{\int {\rm d}k\; k[\Phi_k]^{\rm p+s}_{\rm w\text{-}surface}\,[\mu_{\rm en}(k)/\rho]_{\rm air}}, \tag{2.7}$$

where $[\Phi_k]^{\rm p+s}_{\rm w\text{-}surface}$ is the photon fluence spectrum at the entrance surface, $[\Phi_k]^{\rm p}_{\rm air}$ is the (primary) incident spectrum free-in-air, and $[\mu_{\rm en}(k)/\rho]$ is the mass energy-absorption coefficient in air or water (depending on subscript), for photons of energy k. The spectra entering into the above calculations can be determined by applying the Monte Carlo method, using a water phantom to simulate the entrance surface spectrum, and an analytical x-ray source model to simulate the incident photon beam.

A convenient approach for determining the backscatter factor and the mass energy–absorption coefficient ratio for a given clinical x-ray beam quality Q, is to use pre-calculated data for mono-energetic photons of energy k (Benmakhlouf *et al.*, 2011),

$$B_{\rm air}(Q) = \frac{\int {\rm d}k\; k[\Phi_k]^{\rm p}_{\rm air}\,[\mu_{\rm en}(k)/\rho]_{\rm air}\,B_{\rm air}(k)}{\int {\rm d}k\; k[\Phi_k]^{\rm p}_{\rm air}\,[\mu_{\rm en}(k)/\rho]_{\rm air}}, \tag{2.8}$$

$$[\mu_{\rm en}(Q)/\rho]^{\rm p+s}_{\rm w,air} = \frac{\int {\rm d}k\; k[\Phi_k]^{\rm p}_{\rm air}\,[\mu_{\rm en}(k)/\rho]^{\rm p+s}_{\rm w,air}}{\int {\rm d}k\; k[\Phi_k]^{\rm p}_{\rm air}}, \tag{2.9}$$

where $B_{\rm air}(k)$ and $[\mu_{\rm en}(k)/\rho]^{\rm p+s}_{\rm w,air}$ are, respectively, the backscatter factor and the mass energy–absorption coefficient ratio for photons of energy k. Besides the pre-calculated mono-energetic data entering into the above calculations, the incident x-ray spectrum free-in-air ($[\Phi_k]^{\rm p}_{\rm air}$) is required, which can be determined using an analytical x-ray source model.

When performing the above calculations, it is worth recalling that the backscatter spectrum at the entrance surface depends on a number of factors, such as the x-ray field size, the source-to-surface distance, the simulated phantom thickness (Benmakhlouf *et al.*, 2012), the presence of cranial bone (Omar *et al.*, 2014), and the x-ray beam quality (e.g., tube voltage and beam filtration). Aspects such as these need to be considered when determining the patient entrance surface dose for a specific clinical situation. Andreo (2019) has made available an extensive set of data that can be used for the dosimetry of low- and medium-energy kilovoltage x rays.

2.2 X-ray beam modelling

In order to determine the radiation dose delivered from a medical exposure, and to ensure optimal x-ray imaging performance (according to the ALARA principle), a method for estimating the energy distribution (i.e., the spectrum) of x rays emitted from an x-ray tube is required. The spectrum emitted from an x-ray tube consists of bremsstrahlung and characteristic x-rays produced by electrons incident upon a metallic target, that is, the x-ray tube anode. A complete x-ray beam model should therefore take into account the energy and angular distribution of both bremsstrahlung and characteristic x rays; the basic physics of these two processes is summarized in the next two sections.

Different approaches for predicting the x-ray spectrum have been proposed. Perhaps the most accurate method is to perform MC simulations of the electron-photon transport in the x-ray target (i.e., the x-ray tube anode). Such calculations are, however, impractical for many applications due to the heavy computational burden. A useful alternative may then be a more efficient deterministic spectrum model based on interpolation of experimental data (Boone and Seibert, 1997), interpolation of precomputed results from MC simulations (Hernandez and Boone, 2014), or based on first-principles calculations. Although each approach has its merits, only the latter attempts to describe the underlying physics of x-ray production.

The very first x-ray emission models were formulated by Kramers (1923), and Bethe and Heitler (1934), from principles of classical electrodynamics and rigorous quantum mechanical calculations, respectively. Their models were, however, inherently limited as the production and filtration of bremsstrahlung in the x-ray target were based on simplified approximations. Birch and Marshall (1979) suggested a different approach, in which first-principle calculations are combined with experimental data. Their semi-empirical spectrum model has found broad practical application in the form of a spectrum calculation software (Cranley *et al.*, 1997). Poludniowski and Evans (2007) made further improvements by considering the transport of electrons in the x-ray target in greater detail, using MC calculations to describe the depth and energy distribution of electrons. Their approach was implemented in the widely-used tungsten spectrum calculation software SpekCalc (Poludniowski *et al.*, 2009), and more recently in the spectrum software toolkit SpekPy v1 (Bujila *et al.*, 2020).

Although the above models have generally been successful, their validity for certain applications has been challenged. Kákonyi *et al.* (2009) concluded that the emission angles predicted by Birch and Marshall (1979), and Poludniowski (2007), were in disagreement with MC calculations due to the assumption that the angular distribution of bremsstrahlung production is uniform. This assumption stems from the rationale that electrons incident upon an x-ray target promptly attain a diffuse directional distribution

due to multiple scattering, and thereby effectively mask the intrinsic bremsstrahlung angular distribution. Furthermore, these models do not consider in detail the depth of characteristic x-ray production in the x-ray target. These limitation have been pointed out as reasons why such models fail to accurately predict x-ray emission for small take-off angles[1] (Bhat *et al.*, 1999). It should be noted that the angular distribution of the x-ray emission is relevant for modelling of the so-called (anode) heel effect. The heel effect has been shown to affect the entrance surface air kerma by as much as 40% for x-ray beams used in interventional radiology (Rana *et al.*, 2012), which exceeds the recommended 7% accuracy in dosimetry when tissue reactions are expected (IAEA TRS-457; Alm-Carlsson *et al.*, 2007).

2.2.1 Bremsstrahlung

The emission of bremsstrahlung photons occurs when charged particles decelerate in an electric field due to Coulomb interactions. In an x-ray tube this process takes place inside a metallic x-ray target (the x-ray tube anode), where electrons interact with the Coulomb field of target nuclei and atomic electrons.

Consider an electron with kinetic energy E travelling in direction $\hat{\mathbf{\Omega}}_\mathbf{e}$. As it decelerates, the loss in kinetic energy, k, is emitted by a bremsstrahlung photon in direction $\hat{\mathbf{\Omega}}_\boldsymbol{\gamma}$, leaving the electron with kinetic energy of $E - k$ (illustrated in fig. 2.1). Assuming isotropic medium, and unpolarized electrons and photons, the photon emission direction can be expressed in terms of the polar angle between the initial direction of the electron and the direction of the emitted photon, $\cos\theta = \hat{\mathbf{\Omega}}_\mathbf{e} \cdot \hat{\mathbf{\Omega}}_\boldsymbol{\gamma}$. Hence, the bremsstrahlung process for a material with an atomic number Z can be described by an atomic cross section double differential in photon energy and photon emission angle (Kissel *et al.*, 1983),

$$\frac{\mathrm{d}^2\sigma_{\mathrm{br}}(k, \hat{\mathbf{\Omega}}_\mathbf{e} \cdot \hat{\mathbf{\Omega}}_\boldsymbol{\gamma}; Z, E)}{\mathrm{d}k \, \mathrm{d}\hat{\mathbf{\Omega}}_\boldsymbol{\gamma}} = \frac{Z^2}{\beta^2} \frac{1}{k} \chi(k; Z, E) \, S(\hat{\mathbf{\Omega}}_\mathbf{e} \cdot \hat{\mathbf{\Omega}}_\boldsymbol{\gamma}; k, Z, E), \tag{2.10}$$

where β is the initial electron velocity in units of the speed of light in vacuum, χ is the scaled energy-weighted bremsstrahlung cross section differential in emitted photon energy, and S is the shape function of the bremsstrahlung angular distribution. The right-hand side of the above equation is a convenient partition of the double differential cross section that allows for the photon energy and the photon emission angle to be

[1] The take-off angle is defined as the angle between the x-ray target surface and the direction of the x-ray emission.

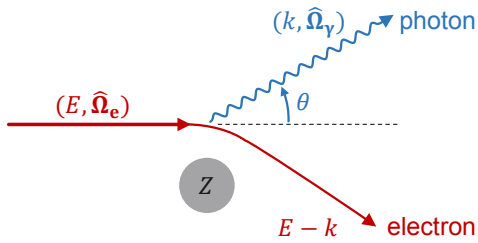

Figure 2.1. Kinematics of bremsstrahlung emission. An electron with kinetic energy E propagating along a unit vector direction $\hat{\mathbf{\Omega}}_\mathrm{e}$ in the Coulomb field of an atom (atomic number Z) generates bremsstrahlung with energy k emitted in direction $\hat{\mathbf{\Omega}}_\gamma$. The polar emission angle is defined as $\cos\theta = \hat{\mathbf{\Omega}}_\mathrm{e} \cdot \hat{\mathbf{\Omega}}_\gamma$.

sampled separately (and efficiently) in numerical applications, as such,

$$\chi(k; Z, E) = \frac{\beta^2}{Z^2} k \frac{\mathrm{d}\sigma_\mathrm{br}(k; Z, E)}{\mathrm{d}k}, \tag{2.11}$$

$$S(\hat{\mathbf{\Omega}}_\mathrm{e} \cdot \hat{\mathbf{\Omega}}_\gamma; k, Z, E) = \frac{\mathrm{d}^2\sigma_\mathrm{br}}{\mathrm{d}k\,\mathrm{d}\hat{\mathbf{\Omega}}_\gamma} \left(\frac{\mathrm{d}\sigma_\mathrm{br}}{\mathrm{d}k} \right)^{-1}. \tag{2.12}$$

Note that the multiplication by the scaling factor $(\beta/Z)^2 k$ is conventionally used because χ varies smoothly with E and k/E for a given element Z.

The electron-nucleus bremsstrahlung cross section is proportional to Z^2, while the much smaller electron-electron bremsstrahlung cross section is proportional to Z (each atomic electron acts as a scattering centre; Tessier and Kawrakow, 2008). The bremsstrahlung process is therefore considerably more important for higher-Z materials, like tungsten, than it is for tissue-like materials.

2.2.2 Characteristic x rays

A characteristic x ray is emitted when an atom with an inner-shell vacancy (i.e., an ion), relaxes through a radiative transition. Atomic shell vacancies are produced in an x-ray target as a result of the following charged and non-charged particle-atom interactions:

- Photon-atom interactions (ph) — An inner-shell electron is ejected in a photoelectric absorption or Compton scattering of a bremsstrahlung photon produced in the target; see fig. 2.2(a, b).
- Inner-shell impact ionization (si) — An electron incident upon the target knocks out an inner-shell electron in an inelastic hard collision; see fig. 2.2(c).

An excited ion with a vacancy in an inner shell can relax through a series of radiative and non-radiative transitions. An x ray with characteristic energy is emitted when an ion is relaxed through a radiative transition; this process is called fluorescence.

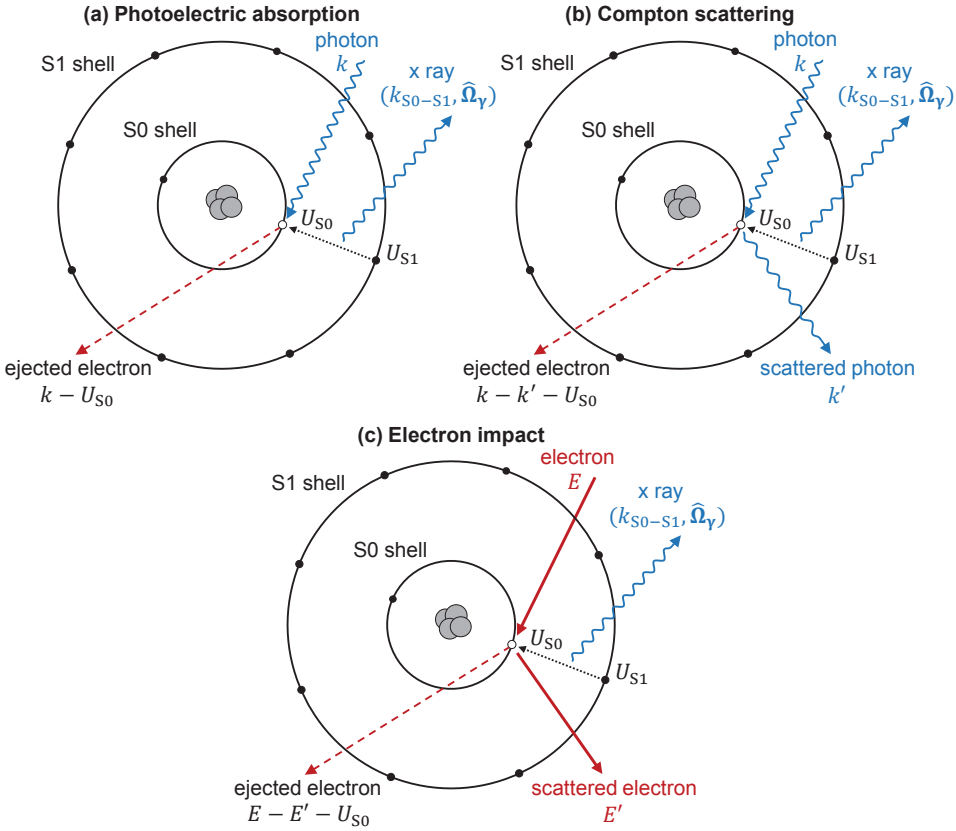

Figure 2.2. Characteristic x-ray emission following inner-shell ionization caused either by photon interactions (a and b) or electron impact (c). With the ejection of an electron from the inner-shell S0, the excited ion relaxes through a radiative transition, resulting in the emission of a characteristic x ray in the direction $\hat{\mathbf{\Omega}}_\gamma$, with energy that is the difference in binding energies between the final and initial shell, $k_{S0-S1} = U_{S0} - U_{S1}$. The energy before and after each of the particle-atom interactions is indicated in the figure, with k' and E' representing the scattered photon and electron kinetic energy, respectively.

Consider a radiative S0–S1 transition: an ion with a vacancy in an inner-shell S0 is filled by an electron from an outer subshell S1, with the excess energy released by the emission of a photon. The probability of a radiative transition (versus a competing non-radiative transition) is given by the fluorescence yield, which is the sum of all radiative

transition probabilities for the given shell,

$$\omega_{\mathrm{S0}}(Z) = \sum_{\mathrm{S1}} P_{\mathrm{S0-S1}}(Z). \tag{2.13}$$

This summation is over all subshells S1 from which electrons can transition to fill a vacancy in S0, for a target atom with atomic number Z. The average number of characteristic x rays emitted per one fluorescence can thus be expressed as,

$$\upsilon_{\mathrm{S0-S1}}(Z) = P_{\mathrm{S0-S1}}/\omega_{\mathrm{S0}}(Z), \tag{2.14}$$

where the characteristic energy is the difference in binding energies between the final and initial shell,

$$k_{\mathrm{S0-S1}} = U_{\mathrm{S0}} - U_{\mathrm{S1}}. \tag{2.15}$$

In a non-radiative S0–S1–S2 transition, an ion with a vacancy in an inner-shell S0 is filled by an electron from an outer subshell S1, and an electron is ejected from the further out subshell S2. The excess energy ($U_{\mathrm{S0}} - U_{\mathrm{S1}} - U_{\mathrm{S2}}$) is released with the ejected electron. Depending on which shells are involved, this process is either an Auger transition (subshells S1 and S2 are in shells different from S0), Coster Kronig transition (S0 and S1 are in the same shell), or Super Coster-Kronig transition (all three subshells are in the same shell).

2.3 The Monte Carlo method

Monte Carlo (MC) methods are a class of numerical techniques distinguished by the use of repeated random sampling to simulate the behaviour of a complex physical or mathematical system. The MC technique can be used to solve problems that are deterministic in principle, but are too complex to be readily solved using conventional deterministic approaches. This was realized in the late 1940s by Stanislaw Ulam at the Los Alamos National Laboratory, who suggested the use of computers and the (Markov Chain) Monte Carlo method to solve neutron diffusion and multiplication problems in fission devices (Eckhardt, 1987). Since then, a substantial increase in computing power has contributed to the MC technique becoming a standard tool for the simulation of complex radiation transport problems. Such simulations are of particular interest in medical physics, in areas such as radiation dosimetry, x-ray imaging, radiotherapy physics, and radiation protection (Raeside, 1976; Andreo, 1991; Verhaegen and Seuntjens, 2003; Rogers, 2006; Seco and Verhaegen, 2013; Morin, 2019).

Various MC systems have been developed over the years for the simulation of photon-electron transport. The different codes can be separated into two categories:

- General-purpose Monte Carlo codes – coupled transport of electrons and photons for a wide range of energies, in arbitrary materials constructed in non-trivial geometries.
- Specialized Monte Carlo codes – transport of photons and/or electrons for specific energies and materials relevant for a particular problem, such as patient dosimetry in x-ray imaging.

Both kinds of codes can be useful, depending on the radiation transport problem considered. The main MC approach used throughout this work is the PENELOPE (Salvat, 2014) general-purpose MC system. Additional MC calculations have been performed using the EGSnrc (Kawrakow *et al.*, 2017) general-purpose MC system, and the specialized MC package PCXMC (Servomaa and Tapiovaara, 1998). Although both of the general-purpose MC systems implement the transport of electrons and photons based on detailed theoretical models for the interaction of particles with matter, they make use of different physics data and transport algorithms. The results obtained using the different codes therefore complement each other. The MC package PCXMC specializes in the simulation of organ absorbed doses for patient dosimetry in diagnostic and interventional radiology, using simplified (and computationally efficient) physics models for the radiation transport. A more in-depth description of the MC systems used in this work is provided in the sections below (sections 2.3.1 to 2.3.3).

2.3.1 PENELOPE

PENELOPE (PENetration and Energy LOss of Positrons and Electrons) is a general-purpose MC system for the simulation of coupled electron-photon transport in the energy range 50 eV to $\sim$1 GeV (Salvat, 2014). Particle-atom interaction mechanisms are simulated using differential cross sections (DCS) obtained from first-principles calculations, semiempirical formulas, and evaluated databases. The cross sections are expressed either numerically or by analytical formulas with parameters fitted to available theoretical or experimental data. It is emphasized that PENELOPE and the DCS used have been validated extensively for simulation of kilovoltage x-ray emission (e.g., Tian *et al.*, 2009; Salvat *et al.*, 2006; Llovet *et al.*, 2014; García-Alvarez *et al.*, 2018). The 2014 version of the PENELOPE MC system has been used throughout this work, along with the main user code *penmain*, or the user code *penEasy* (Sempau *et al.*, 2011), depending on the radiation transport problem considered. The models and physics data implemented in the version used are summarized below.

The electron interactions pertinent to this work are elastic scattering, inelastic collisions (including inner-shell impact ionization), and bremsstrahlung. PENELOPE simulates elastic scattering using DCS based on relativistic (Dirac) partial-wave expansion pre-calculated with the program ELSEPA (Salvat *et al.*, 2005). ELSEPA implements one of the most reliable theories for elastic scattering available (ICRU, 2007), and is the basis for the NIST (National Institute of Standards and Technology, USA) electron elastic-scattering cross-section database (Jablonski *et al.*, 2016). It should be noted that throughout this work, the elastic scattering was simulated in detail instead of using a multiple-scattering approach. This was done by setting equal to zero the PENELOPE parameter C1 (and C2), which governs the conditions for using detailed and class II (mixed) electron track simulations. Inelastic collisions are accounted for by DCS determined by calculations in the plane-wave (first) Born approximation with the Sternheimer-Liljequist generalized oscillator strength model (Liljequist, 1983), including the density effect correction. Inelastic collisions resulting in inner-shell ionization are handled using DCS for electron impact calculated by Bote and Salvat (2008) in the distorted-wave (first) Born approximation and the plane-wave (first) Born approximation for low and high initial electron energies, respectively. Their model is extensively validated against experimental results (Llovet *et al.*, 2014).

The bremsstrahlung energy and angle are sampled separately based on the partitioning of the double differential cross section expressed by eq. (2.10). The photon energy is sampled using cross section from the NIST database (Seltzer and Berger, 1985), which for electron kinetic energies up to 2 MeV contains results by Pratt *et al.* (1977), who performed relativistic partial-wave calculations of bremsstrahlung emitted in the electric field generated by a static screened Coulomb potential representing the nucleus. This approach is considered to be the most reliable description of bremsstrahlung presently available. The NIST database accounts for bremsstrahlung emitted in the field of bound electrons based on calculations using the Born-approximation formula (including a multiplicative Coulomb correction factor) by Haug (1975) for an unscreened free electron, supplemented with a correction for screening and binding effects based on the work of Wheeler and Lamb (1939). The intrinsic bremsstrahlung angular distribution is accounted for using an approximate analytical parametrization (Acosta *et al.*, 2002) fitted closely to benchmark results obtained by Kissel *et al.* (1983), who performed partial-wave calculations similar to those by Pratt *et al.* (1977) for the bremsstrahlung photon energy.

The key physics data for the photon transport consists of the following DCS. The photoelectric effect is simulated using subshell-dependent DCS calculated with the program PHOTACS (Sabbatucci and Salvat, 2016), which applies the theory by Scofield (1978) for cross sections renormalized by a screening correction to account for inaccuracies in the central potential used (i.e., the atomic wave function used). This

renormalization is the main difference compared with the cross sections included in the established Evaluated Photon Data Library (EPDL) (Cullen *et al.*, 1997), and in the essentially identical XCOM database (Berger and Hubbell, 1987). Coherent (Rayleigh) scattering is simulated using DCS that are the product of the classical Thomson cross section and the nonrelativistic form factor plus the dispersion correction to the form factor extracted from EPDL. Incoherent (Compton) scattering is accounted for using DCS calculated based on the Impulse Approximation by Ribberfors (1975), which accounts for electron-binding effects and Doppler broadening of the Compton line, with an analytical approximation for the subshell Compton profiles by Brusa *et al.* (1996).

PENELOPE simulates atomic relaxations using radiative and non-radiative transition probabilities from the Evaluated Atomic Data Library (EADL) of Perkins *et al.* (1991). The database contains values for the transition of ionized atoms with a single vacancy in one of the electron shells, calculated using the independent electron model with the Dirac-Hartree-Fock-Slater potential. The results have been further adjusted to reproduce the Z-dependence of the effective fluorescence yield, that is, the number of x rays emitted in the filling of a parent vacancy and any of its daughter vacancies in other subshells of the same shell. The characteristic x-ray energy emitted in a radiative transition is from the compilation by Deslattes *et al.* (2003) of theoretical calculations and selected experimental data.

2.3.2 EGSnrc

EGSnrc (Electron Gamma Shower; National Research Council - Canada) is a general-purpose MC system for the simulation of coupled electron-photon transport for energies of a few tens of keV up to a few hundred GeV (Kawrakow *et al.*, 2017). EGSnrc is a well-established MC transport code in the field of medical physics, and has, like PENELOPE, been evaluated by AAPM TG 195 (Sechopoulos *et al.*, 2015) for radiology applications. EGSnrc differs from PENELOPE in that it includes various physics models and cross section data that can be selected by the user based on the radiation transport problem at hand. The 2017 version of the EGSnrc MC system has been used throughout this work, along with the user code *BEAMnrc* (Rogers *et al.*, 1995). A summary of the models and physics data settings used for the MC simulations performed in this work, are given below.

The electron transport has been simulated in detail instead of using a multiple-scattering approach, i.e., an analogue technique for elastic scattering. This was done by employing the exact boundary crossing algorithm and the PRESTA-II electron-step algorithm with an exceedingly large skin depth. EGSnrc simulates elastic scattering using DCS that are the product of the screened Rutherford cross section (modified slightly to account for angular deflections due to sub-threshold processes) and the so-

called Mott correction obtained by partial-wave expansion of the Dirac equation in the nuclear field screened by atomic electrons (Motz *et al.*, 1964). Discrete inelastic collisions are described by the Møller cross section (Møller, 1932). Inelastic collisions resulting in inner-shell ionization (i.e., electron impact ionization) have throughout this work been simulated using the PENELOPE physics option, which implements cross sections by Bote and Salvat (2008). It is worth mentioning that for the simulations performed using the XTUBE module in BEAMnrc, the internal boundary tolerance parameter, $BDY_TOL, was changed from the default value to 5×10^{-7} cm, in order to correctly simulate electron backscatter at boundaries (Ali and Rogers, 2008*b*).

EGSnrc simulates bremsstrahlung emission in a similar manner to PENELOPE, with the energy and angle sampled separately based on the partitioning of the double differential cross section expressed by eq. (2.10). The photon energy is sampled using DCS from the NIST database (Seltzer and Berger, 1985). Different options are provided for the intrinsic bremsstrahlung angular distribution (i.e., the shape function): (i) the so-called SIM shape function takes the angle-dependent leading term of the 2BN (plane-wave first Born approximation, no screening) double differential bremsstrahlung cross section (Koch and Motz, 1959), and (ii) KM which is a modification of 2BS (high-energy result, screened nucleus) to emulate 2BN. The effects of using different shape functions in calculations of x-ray emission are analysed in section 4.1.1.

The photon transport is based on the following DCS. The photoelectric effect is simulated based on the cross sections in the XCOM database (Berger and Hubbell, 1987), which have been calculated using the same formalism as used by Scofield (1973) for unrenormalized cross sections. Recall that PENELOPE uses cross sections renormalized by a screening correction. EGSnrc has in a more recent version also made available the use of renormalized cross sections for the photoelectric effect. Coherent (Rayleigh) scattering is simulated using DCS that are the product of the classical Thomson cross section and the relativistic form factor by Hubbell and Øverbø (1979), disregarding the dispersion correction to the form factor. Incoherent (Compton) scattering is simulated using DCS based on the same theory as implemented by PENELOPE, except for a minor improvement to the photon scattering angle by a more detailed evaluation of the incoherent scattering function.

The simulation of radiative transitions has been performed by setting the internal parameter $EADL_RELAX to “true”, which enables explicit treatment of all atomic electron shell transitions based on the transition probabilities and energies included in EADL (Perkins *et al.*, 1991). The default setting in EGSnrc ($EADL_RELAX set to “false”) accounts in detail only for K- and L-shell transitions, while the transitions to and from M- and N-shells are treated in an average way, which has been shown to introduce substantial errors in characteristic L-lines (Watson and Seuntjens, 2016).

2.3.3 PCXMC

PCXMC (Personal Computer program for X-ray Monte Carlo) is a commercial MC system for calculating patients' organ absorbed doses and effective doses for radiological examinations (Servomaa and Tapiovaara, 1998). The user can specify parameters that describe the patient size, x-ray beam geometry, x-ray spectrum, and the number of incident x rays. PCXMC simulates the photon transport in one of the slightly modified and updated stylized (mathematical) hermaphrodite phantom models of Cristy and Eckerman (1987) (newborn, 1, 5, 10, 15, and 30 years old), with the incident photon energy distributed according to the deterministic x-ray spectrum model of Birch and Marshall (1979). Note that the energy transferred to electrons ejected in photon-atom interactions is assumed to be deposited locally. This assumption is valid for most of the organs and tissues considered, given that the electron range is much smaller than the dimensions of the organs. However, as was pointed out in section 2.1.1, this is not the case for red bone marrow due to the absence of charged particle equilibrium in the small cavities of trabecular bone. PCXMC therefore calculates the dose to red bone marrow using the photon energy dependent kerma-to-dose conversion factors produced by Kerr and Eckerman (1985).

The photoelectric effect, coherent (Rayleigh) and incoherent (Compton) scattering, are simulated using the Storm and Israel (1970) cross sections, with atomic form factors and incoherent scattering functions from Hubbell *et al.* (1975). PCXMC does not simulate atomic relaxations, assuming instead that the energy released in radiative and non radiative transitions is absorbed locally. It is emphasized that the simplified photon transport allows for more efficient, albeit less accurate, calculations compared with using the more comprehensive particle transport provided by general-purpose MC systems.

Chapter 3

Framework for patient dose estimation

Accurate patient dosimetry for interventional image-guided therapy (IGT) has traditionally been a challenge due to lack of information about the physical context of the various x-ray exposures performed during such procedures. Recall that image-guided therapy x-ray systems modulate the energy and intensity of the x-ray beam to ensure an adequate image quality regardless of which part of the body is imaged (Rauch *et al.*, 2012), i.e., Intensity Modulated Diagnostic Radiology (IMDR). In order to make available the information needed for more accurate radiation dose assessment, the U.S. National Electrical Manufacturers Association (NEMA) has introduced radiation dose structured reports (RDSR) as part of the Digital Imaging and Communications in Medicine (DICOM) standard. RDSR is, in accordance with IEC 60601-2-43 (IEC, 2010), required to be supported on newly manufactured x-ray systems.

Based on the exposure-related data contained in RDSR, a framework for systematic estimation of organ absorbed doses was developed in Paper I. The framework is consistent with well-established air kerma based dosimetry formalisms for medical x-ray imaging (see section 2.1), and consists of the following steps (see fig. 3.1):

- Reconstructing the geometrical relation between the projected x-ray beam and the patient's anatomy.
- Calculating the incident air kerma (i.e., without backscatter).
- Converting the incident air kerma into organ absorbed dose, considering different photon-atom interaction processes in tissue.

The first two steps result in the incident air kerma being determined from the reference air kerma free-in-air (K_{ref}) reported in RDSR for each individual x-ray exposure part of a performed x-ray procedure. The final step can be achieved by different means, such as: (i) applying precalculated factors that convert incident air kerma into organ

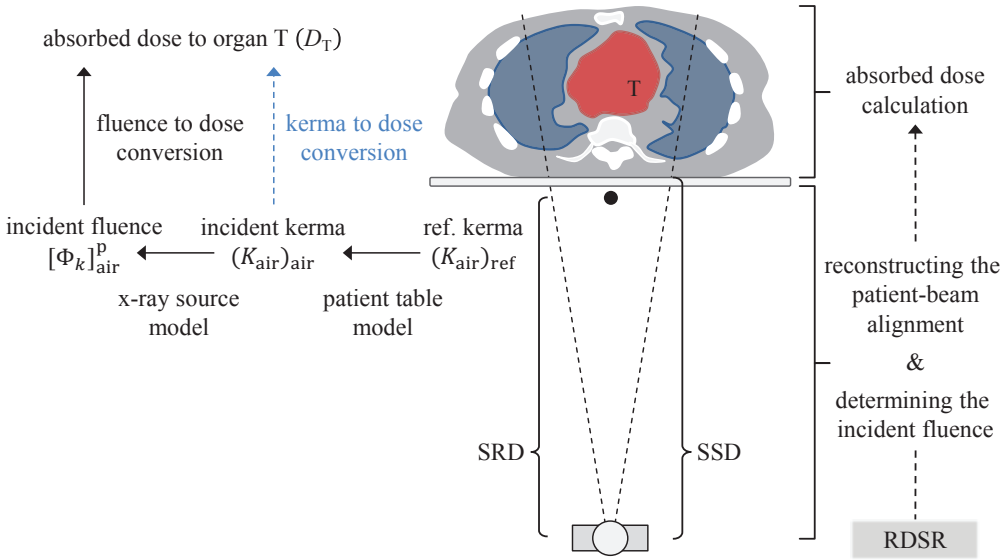

Figure 3.1. Framework for patient dose estimation based on data contained in radiation dose structured reports (RDSR). The calculation workflow consists of converting the air kerma free-in-air determined in a reference point, K_{ref}, into the incident photon fluence differential in energy, $[\Phi_k]^{\mathrm{p}}_{\mathrm{air}}$, using an x-ray source model and accounting for the patient table attenuation. Also shown in an alternative approach that consists of converting air kerma directly into organ absorbed dose using precalculated conversion factors (blue dashed arrow). SRD and SSD is the source-to-reference and source-to-surface distance, respectively. (Adapted from Paper I, Omar *et al.* (2016))

absorbed dose, or (ii) using the Monte Carlo method along with an x-ray source model (to determine the incident x-ray fluence) for the calculation of energy deposited in an anthropomorphic phantom. In order to perform such calculations, the geometrical relation between the projected x-ray beam and the patient's anatomy needs to be reconstructed.

3.1 Reconstructing the patient-beam alignment

In order to determine organ absorbed doses, the location of the x-ray beam in relation to the patient anatomy has to be considered. The exposure geometry can be reconstructed by matching the orientation and position of a suitable anthropomorphic phantom model to the patient's position and orientation on the table top. As part of the framework developed in Paper I, a novel method for patient-beam alignment was introduced. The

so-called target-centric approach uses DICOM RDSR data to infer the patient position relative to the x-ray system's frame of reference, by identifying the primarily imaged body region (e.g., the heart for cardiovascular interventions). The target organ can be located by taking advantage of the fact that during an x-ray procedure most of the irradiation time is dedicated to visualizing the target region.

Using RDSR data, the location of the (x-ray beam/system) isocenter relative to the patient table head end position (position $[0, 0]$ in fig. 3.2) can be formulated as a function of irradiation time,

$$\mathbf{r_{iso}}(t) = \mathbf{r_b}(t) - \mathbf{r_t}(t), \tag{3.1}$$

where $\mathbf{r_b}$ and $\mathbf{r_t}$ are, respectively, the beam isocenter position and the table head end position in the x-ray system's frame of reference. The position of the target organ [$\mathbf{r_{target}} = (x_{\text{target}}, y_{\text{target}}, z_{\text{target}})$] can then be estimated as the median position of the isocenter [$\mathbf{r_{iso}} = (x_{\text{iso}}, y_{\text{iso}}, z_{\text{iso}})$], as,

$$\begin{aligned} x_{\text{target}} &= \text{median}(\{x_{\text{iso}}(t) \mid t \in \mathcal{X}\}), \\ y_{\text{target}} &= \text{median}(\{y_{\text{iso}}(t) \mid t \in \mathcal{X}\}), \\ z_{\text{target}} &= \text{median}(\{z_{\text{iso}}(t) \mid t \in \mathcal{X}\}), \end{aligned} \tag{3.2}$$

where the set $\mathcal{X}$ excludes time periods (i.e., exposure series) when the exposure is presumably not aimed at the visualization of the target region, e.g., during catheter insertion. This may for instance be the exclusion of time periods when the isocenter is located outside of the limitations imposed by a head fixation apparatus used for neurovascular procedures. Note that the median is used instead of the mean in the above equations to improve the accuracy in the estimated target organ position by reducing the impact of outlying isocenter positions.

With the patient's target organ located in the x-ray system's frame of reference, the exposure geometry can be reconstructed in a computational frame of reference by translation of the coordinate system origin,

$$\mathbf{r}_{\mathbf{iso}}^{\mathbf{comp}}(t) = \mathbf{r}_{\mathbf{target}}^{\mathbf{comp}} + \Big(\mathbf{r_{iso}}(t) - \mathbf{r_{target}}\Big), \tag{3.3}$$

where $\mathbf{r}_{\mathbf{iso}}^{\mathbf{comp}}(t)$ and $\mathbf{r}_{\mathbf{target}}^{\mathbf{comp}}$ are, respectively, the position of the isocenter and the target organ in the phantom model used.

The suggested approach differs from previous work in that it is patient-specific. Previous applications have relied on the use of a standard position for the patient on the table top (Khodadadegan *et al.*, 2011; Johnson *et al.*, 2011), or have assumed that all x-ray exposures are centred on the target organ (Karambatsakidou *et al.*, 2009). Such assumptions may introduce errors in patient dose calculations, as the dose may

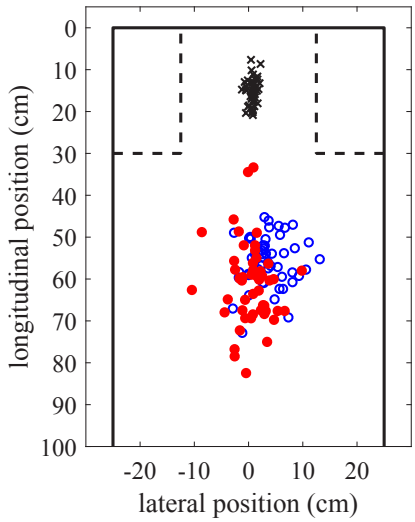

Figure 3.2. Target organ positions projected onto the patient table, localised using clinical DICOM images for 50 neurovascular (×), adult (○) and paediatric (●) cardiology procedures. The contours of the table top (line) and the head fixation apparatus (dashed line) are outlined for illustrative purposes. (Adapted from Paper I, Omar *et al.* (2016))

be calculated for other organs than the ones actually exposed. Figure 3.2 shows target organ positions projected onto the patient table, localised using clinical DICOM images for various interventional x-ray procedures. The large spread observed was found to be due to variations in the positioning of the patient on the table top, rather than being due to variations in the patient size.

In Paper I, the method developed for locating the target organ position (i.e., the target-centric approach) was evaluated for 150 patients, by comparing with results obtained assuming a standardized position for the patient on the table top. The target-centric approach was shown to be distinctly more accurate in locating the primarily irradiated organs (accurate to within 4.3 cm) than when assuming a standardized position (within 24 cm). The effect on patient dose estimations was evaluated by using the framework developed in Paper I, along with the PCXMC MC system (described in section 2.3.3). Organ absorbed doses were calculated using both the target-centric approach and assuming a standardized position for the patient on the table top, as well as using clinical DICOM images to determine the ground truth for the reconstruction of the patient-beam alignment. The target-centric approach was generally within 5% of the ground truth for the primarily irradiated organs, while assuming a standardized patient position resulted in a percent difference exceeding 30% for several organs.

3.2 Determining the incident air kerma

The incident air kerma, i.e., the air kerma free-in-air on the central-axis at the patient entrance surface, is one of the principal quantities for patient dosimetry in the IAEA TRS-457 code of practice (Alm-Carlsson *et al.*, 2007). For image-guided therapy procedures the location of the patient skin is usually not tracked, which is why a reference air kerma free-in-air, $(K_{\mathrm{air}})_{\mathrm{ref}}$, is reported instead. The reference point is conventionally located on the central-axis, 15 cm from the isocenter towards the x-ray tube. The incident air kerma can be determined from the reference point kerma,

$$(K_{\mathrm{air}})_{\mathrm{air}} = (K_{\mathrm{air}})_{\mathrm{ref}}\, f_{\mathrm{table}}\, (d_{\mathrm{SRD}}/d_{\mathrm{SSD}})^2, \tag{3.4}$$

where SRD and SSD are the source-to-reference distance and the source-to-surface distance, respectively. The latter is typically unknown and not reported in RDSR, which is why it has to be determined by other means, such as ray tracing to find the distance from the x-ray source to the surface of a phantom model that emulates the patient body. The table transmission factor, f_{table}, accounts for the attenuation of the patient table, and can be determined either experimentally, or analytically,

$$f_{\mathrm{table}} = \frac{\int \mathrm{d}k\; k[\Phi_k]^{\mathrm{p}}_{\mathrm{ref}}\, [\mu_{\mathrm{en}}(k)/\rho]_{\mathrm{air}}\, F_{\mathrm{table}}(k, \theta_{\mathrm{iso}}, \phi_{\mathrm{iso}})}{\int \mathrm{d}k\; k[\Phi_k]^{\mathrm{p}}_{\mathrm{ref}}\, [\mu_{\mathrm{en}}(k)/\rho]_{\mathrm{air}}}, \tag{3.5}$$

where $[\mu_{\mathrm{en}}(k)/\rho]_{\mathrm{air}}$ is the mass energy-absorption coefficient in air for photons of energy k, $[\Phi_k]^{\mathrm{p}}_{\mathrm{ref}}$ is the photon fluence spectrum at the reference point (p indicates primary photons, i.e., not including backscatter from the table), and $F_{\mathrm{table}}(k, \theta_{\mathrm{iso}}, \phi_{\mathrm{iso}})$ is the mono-energetic transmission through the patient table,

$$F_{\mathrm{table}}(k, \theta_{\mathrm{iso}}, \phi_{\mathrm{iso}}) = \exp\left(-\sum_i [\mu(k)/\rho]_i (\rho\ell)_i \sqrt{\tan^2\theta_{\mathrm{iso}} + \tan^2\phi_{\mathrm{iso}} + 1} \right), \tag{3.6}$$

where $[\mu(k)/\rho]_i$ is the photon mass attenuation coefficient for material i, and $(\rho\ell)_i$ is the mass thickness of material i. Note that the above equation accounts for the increased oblique path length traveled by x rays through the patient table, using the angles θ_{iso} and ϕ_{iso} to specify the rotation of the x-ray beam about the isocentre. The mass thickness of the table can be approximated by fitting results calculated using eq. (3.6) (carbon and water equivalent thickness being the parameters fitted), to air kerma transmission measurements for clinically relevant beam qualities. Results obtained in this manner are shown in fig. 3.3. It is worth noting that the above approach ignores the contribution to the incident kerma from photons forward scattered in the patient table. This can be factored into the calculations using a primary-to-scatter ratio that has been determined either experimentally, or by MC simulations (Vijayan *et al.*, 2018).

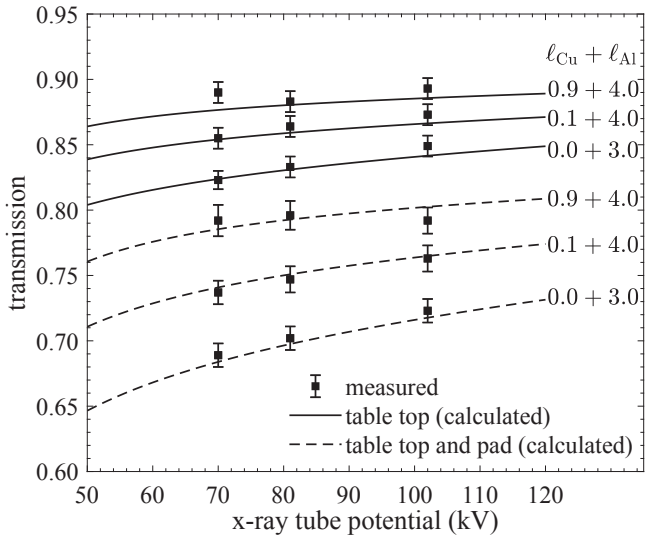

Figure 3.3. Air kerma transmission factors for a patient table used with an Artis Zee (Siemens Healthineers, Forchheim, Germany) interventional image-guided therapy x-ray system. The results correspond to measurement for a posterior-anterior projection, and calculations using eq. (3.5) with an angle of incidence of ($\theta_{\mathrm{iso}} = 0, \phi_{\mathrm{iso}} = 0$), a mass thickness of 3.0 mm carbon (2.0 g cm^{-3}) and 1.0 mm water (epoxy resin) for the table top, and a mass thickness of 5 mm water (PU foam) for the pad. The uncertainty bars correspond to one standard deviation. The x-ray beam filtration is specified in millimetre copper and aluminimum ($\ell_{\mathrm{Cu}} + \ell_{\mathrm{Al}}$).

In order to perform organ absorbed dose calculations using the Monte Carlo method, the incident x-ray spectrum has to be determined. This can be achieved as follows: (i) using an x-ray spectrum model to determine $[\Phi_k]^{\mathrm{p}}_{\mathrm{ref}}$, (ii) accounting for the filtration of x rays in the patient table, and (iii) adjusting the x-ray fluence to match the reported reference air kerma, $(K_{\mathrm{air}})_{\mathrm{ref}}$. This can be formulated analogue to eq. (3.4), as,

$$[\Phi_k]^{\mathrm{p}}_{\mathrm{air}} = \frac{[\Phi_k]^{\mathrm{p}}_{\mathrm{ref}}\,(K_{\mathrm{air}})_{\mathrm{ref}}}{\int \mathrm{d}k\; k[\Phi_k]^{\mathrm{p}}_{\mathrm{ref}}[\mu_{\mathrm{en}}(k)/\rho]_{\mathrm{air}}}\, F_{\mathrm{table}}(k, \theta_{\mathrm{iso}}, \phi_{\mathrm{iso}})\,(d_{\mathrm{SRD}}/d_{\mathrm{SSD}})^2. \qquad (3.7)$$

Notice that for the calculations described in this section, an x-ray spectrum model is required. The development of such a model is the subject of the next chapter.

Chapter 4

X-ray source model

This chapter summarizes the development of a deterministic model for the energy and angular distribution of x rays emitted from an x-ray tube. The calculation of the x-ray emission spectrum, that is, the x-ray fluence differential in photon energy k per incident electron with kinetic energy E_0, was given in a general form in Paper V,

$$\begin{aligned}\Phi_k(k, \mathbf{r}; Z, E_0) &= \Phi_k^{\mathrm{br}} + \Phi_k^{\mathrm{ch}} \\ &= G(\mathbf{r}) H(k, \hat{\mathbf{\Omega}}_{\boldsymbol{\gamma}}) \left((N_{k,\hat{\mathbf{\Omega}}_{\boldsymbol{\gamma}}}^{\mathrm{br}} + N_{k,\hat{\mathbf{\Omega}}_{\boldsymbol{\gamma}}}^{\mathrm{ch}})(k, \hat{\mathbf{\Omega}}_{\boldsymbol{\gamma}}; Z, E_0) \right),\end{aligned} \tag{4.1}$$

where $N_{k,\hat{\mathbf{\Omega}}_{\boldsymbol{\gamma}}}^{\mathrm{br}}$ and $N_{k,\hat{\mathbf{\Omega}}_{\boldsymbol{\gamma}}}^{\mathrm{ch}}$ are, respectively, the number of bremsstrahlung and characteristic x rays emerging from a target of atomic number Z, differential in photon energy k and emission direction $\hat{\mathbf{\Omega}}_{\boldsymbol{\gamma}}$. The conversion to fluence (at a point $\mathbf{r}$ in the x-ray field) and the attenuation of filters is accounted for, respectively, by

$$G(\mathbf{r}) = \|\mathbf{r}\|^{-2} \quad \text{and} \quad H(k, \hat{\mathbf{\Omega}}_{\boldsymbol{\gamma}}) = \exp\left(-\sum_i \mu_i(k)\, t_i(\hat{\mathbf{\Omega}}_{\boldsymbol{\gamma}}) \right), \tag{4.2}$$

where $t_i(\hat{\mathbf{\Omega}}_{\boldsymbol{\gamma}})$ is the thickness of a filter material i in the emission direction $\hat{\mathbf{\Omega}}_{\boldsymbol{\gamma}}$, and μ_i is the linear attenuation coefficient.

In order to evaluate eq. (4.1), the production of both bremsstrahlung and characteristic x rays in the x-ray target (i.e., the x-ray tube anode) has to be considered. The model for bremsstrahlung production is presented in section 4.1 (Paper V), and the model for characteristic x-ray production is presented in section 4.2 (Paper III). In section 4.3 the complete model is compared with MC-calculated results, published measured spectra, and models developed by other authors (Paper VI).

4.1 Bremsstrahlung production

Recall the notations used to describe bremsstrahlung emission in section 2.2.1, that is, a bremsstrahlung photon with energy k is emitted in direction $\hat{\mathbf{\Omega}}_{\boldsymbol{\gamma}}$ as an electron with kinetic energy E traveling in direction $\hat{\mathbf{\Omega}}_{\mathbf{e}}$ decelerates in the Coulomb field of an atom (see fig. 4.1). Using these notations, the number of bremsstrahlung photons emerging from a target with atomic number Z and atomic density n (isotropic medium) per incident electron with kinetic energy E_0, can be expressed as,

$$N^{\mathrm{br}}_{k,\hat{\mathbf{\Omega}}_{\boldsymbol{\gamma}}}(k,\hat{\mathbf{\Omega}}_{\boldsymbol{\gamma}};Z,E_0) = n\int_0^{\infty}\mathrm{d}x\int_k^{E_0}\mathrm{d}E\int\mathrm{d}\hat{\mathbf{\Omega}}_{\mathbf{e}}\,N^{\mathrm{e}}_{E,\hat{\mathbf{\Omega}}_{\mathbf{e}}}(x,E,\hat{\mathbf{\Omega}}_{\mathbf{e}};Z,E_0) \times \frac{\mathrm{d}^2\sigma_{\mathrm{br}}(k,\hat{\mathbf{\Omega}}_{\mathbf{e}}\cdot\hat{\mathbf{\Omega}}_{\boldsymbol{\gamma}};Z,E)}{\mathrm{d}k\,\mathrm{d}\hat{\mathbf{\Omega}}_{\boldsymbol{\gamma}}}\,f_{\mathrm{br}}(x,k,\hat{\mathbf{\Omega}}_{\boldsymbol{\gamma}};Z), \quad (4.3)$$

where $N^{\mathrm{e}}_{E,\hat{\mathbf{\Omega}}_{\mathbf{e}}}(x,E,\hat{\mathbf{\Omega}}_{\mathbf{e}};Z,E_0)$ is the number of electrons at depth x in the target per incident electron, differential in the kinetic energy E and direction $\hat{\mathbf{\Omega}}_{\mathbf{e}}$. The filtration of bremsstrahlung by overlying target material can be accounted for in terms of the transmission of photons with energy k emitted in direction $\hat{\mathbf{\Omega}}_{\boldsymbol{\gamma}}$ from a depth x,

$$f_{\mathrm{br}}(x,k,\hat{\mathbf{\Omega}}_{\boldsymbol{\gamma}};Z) = \exp\Big(-\mu(k;Z)\,x\csc\varphi\,\sec\vartheta\Big), \quad (4.4)$$

where μ is the target material's linear attenuation coefficient, φ is the take-off angle (shown in fig. 4.1(b)) defined by $\csc\varphi = \|\mathbf{r}_x+\mathbf{r}_z\|/\|\mathbf{r}_x\|$ and ϑ is the corresponding out-of-plane angle (not shown in the figure) defined by $\sec\vartheta = \|\mathbf{r}\|/\|\mathbf{r}_x+\mathbf{r}_z\|$, given that $\|\mathbf{r}\| \gg x$.

Recall that the double differential bremsstrahlung cross section can be factorized into an energy and angular distribution (see eq. (2.10)). The typical approach of previous analytical x-ray spectrum models (Birch and Marshall, 1979; Tucker *et al.*, 1991; Poludniowski, 2007; Hernández and Fernández, 2016) has been to assume a spherically uniform intrinsic bremsstrahlung angular distribution, thereby reducing eq. (4.3) to the evaluation of a single differential cross section (energy distribution). This assumption stems from the rationale that electrons promptly attain a diffuse directional distribution due to multiple scattering, thereby effectively masking the intrinsic bremsstrahlung angular distribution. The present model differs from previous work in that the intrinsic bremsstrahlung angular distribution is considered in detail. As such, the angular distribution of electrons at depth in the target has to be considered explicitly, rather than assuming diffusion (Bethe and Ashkin, 1953), i.e., a broad angular distribution that does not change with penetration depth.

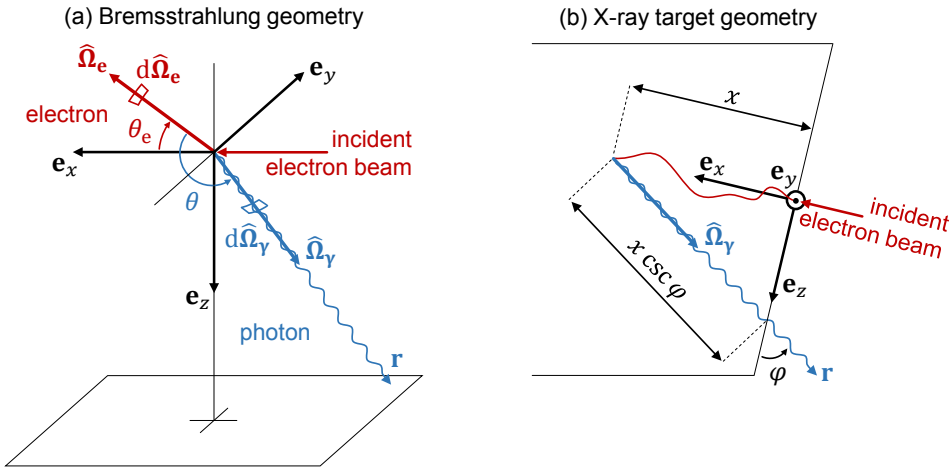

Figure 4.1. Geometry of (a) the bremsstrahlung process, and (b) the emission of x rays from a target (i.e., an x-ray tube anode). Electrons propagating along a unit vector direction $\hat{\mathbf{\Omega}}_\mathbf{e}$ generate photons of energy k emitted in direction $\hat{\mathbf{\Omega}}_\gamma$. The electron propagation direction is specified by the polar angle θ_e relative to the incidence direction, $\mathbf{e}_x$. The photon emission direction is specified by the polar angle between the direction of the emitted photon and the initial electron direction, i.e., $\cos\theta = \hat{\mathbf{\Omega}}_\mathbf{e} \cdot \hat{\mathbf{\Omega}}_\gamma$. Photons generated at depth x in the target are shown in (b) to travel along the take-off angle φ to a point $\mathbf{r}$. (From Paper V, Omar *et al.* (2020*a*))

The electron penetration can be determined by MC calculation of the number of electrons with kinetic energy E crossing a plane at depth x in the direction $\hat{\mathbf{\Omega}}_\mathbf{e}$,

$$N^\mathrm{e}_{E,\hat{\mathbf{\Omega}}_\mathbf{e}}(x, E, \hat{\mathbf{\Omega}}_\mathbf{e}; Z, E_0) = \frac{\mathrm{d}^2 N^\mathrm{e}_\mathrm{pl}(x, E, \hat{\mathbf{\Omega}}_\mathbf{e}; Z, E_0)}{\left|\hat{\mathbf{\Omega}}_\mathbf{e} \cdot \mathbf{e}_x\right| \mathrm{d}E \, \mathrm{d}\hat{\mathbf{\Omega}}_\mathbf{e}}, \tag{4.5}$$

where, $\left|\hat{\mathbf{\Omega}}_\mathbf{e} \cdot \mathbf{e}_x\right| = \left|\cos\theta_\mathrm{e}\right|$, relates the number of electrons at depth x (N^e) to the MC-calculated number of electrons crossing a plane at that depth (N^e_pl), similar to how fluence and planar fluence are related (Andreo *et al.*, 2017).

The described bremsstrahlung model has been implemented in the computational environment MATLAB (available from Omar *et al.* (2020*c*)), with the electron penetration (eq. (4.5)) determined using the PENELOPE MC system. The model was used in Paper V to determine depth and energy distributions of bremsstrahlung produced in tungsten. The results are presented in fig. 4.2, along with results obtained assuming instant electron diffusion (Poludniowski and Evans, 2007), and including MC-calculated results for reference.

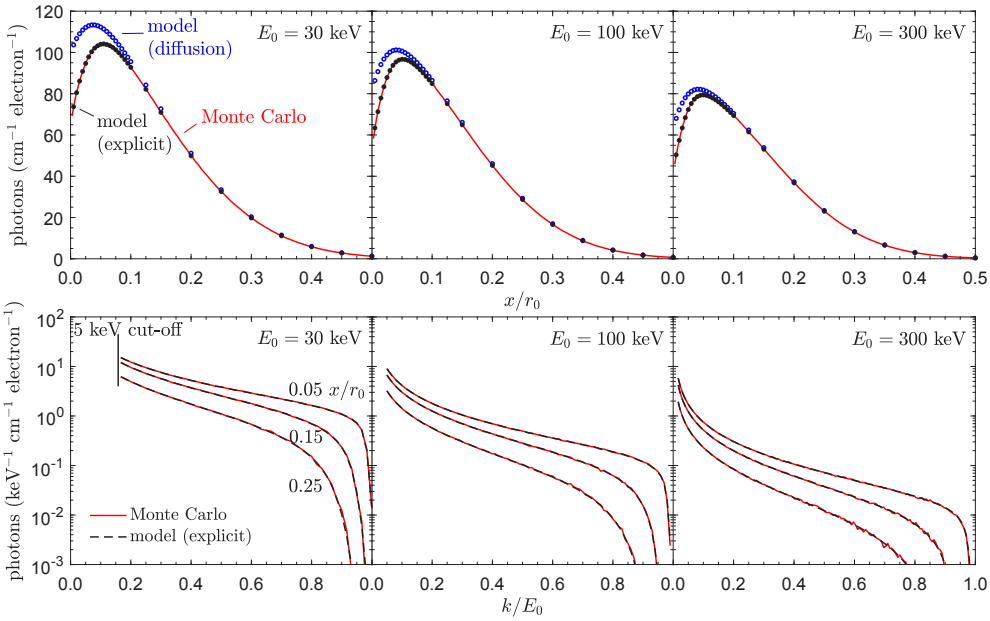

Figure 4.2. Depth and energy distributions of bremsstrahlung produced in tungsten, per incident electron with kinetic energy E_0. The penetration depth and energy are scaled, respectively, by the CSDA range ($x/r_0(E_0)$) and the incident electron energy (k/E_0). Monte Carlo (PENELOPE) calculations are compared with analytical model results obtained by explicitly accounting for the electron angular distribution, and assuming instant diffusion. (From Paper V, Omar *et al.* (2020*a*))

The figure shows that the assumption of instant diffusion (i.e., that electrons instantaneously attain a diffuse directional distribution) introduces errors in the build up region of the target. The amount of bremsstrahlung produced near the target surface is overestimated by more than 30% for low incident electron energies. Using instead the model developed in Paper V, which accounts explicitly for the electron angular distribution, the bremsstrahlung production can be estimated more accurately (within 0.5%). The figure also shows that the model predictions are in excellent agreement with MC results for the energy distribution of the produced bremsstrahlung.

The bremsstrahlung generated within the target has an intrinsic angular distribution which needs to be considered when modeling the x-ray energy leaving the target in a given direction. The intrinsic bremsstrahlung angular distribution, i.e., the shape function (eq. (2.12)), is considered in the next section.

4.1.1 Bremsstrahlung angular distribution

Several fundamentally different theories for the intrinsic bremsstrahlung angular distribution have been proposed in the literature. In Paper II, various shape functions derived from different theories of electron-nucleus bremsstrahlung were implemented in the EGSnrc MC system to evaluate their impact on x-ray emission calculations in the energy range 20–300 kV (i.e., the operational range of most x-ray tubes). As is generally the practice for MC calculations, the electron-electron bremsstrahlung angular distribution was assumed to be the same as that for electron-nucleus bremsstrahlung. The shape functions investigated in Paper II are listed in table 4.1. They correspond to commonly used models in MC and analytical calculations of x-ray emission in the energy range of interest.

Figure 4.3 shows the angular distribution of bremsstrahlung exiting a (minimally) thin tungsten target, calculated using different theories for the intrinsic bremsstrahlung angular distribution. The figure shows that for low incident electron energies only the 2BN Born approximation formula and the KQP (Kissel-Quarles-Pratt) partial-wave results predict that the maximum does not occur at zero degree emission angle. The 2BS Born approximation formula, which was derived using high-energy approximations (extreme-relativistic and small-angle), performs considerably better for higher energies, but fails at lower energies. KM, which is based on 2BS, shows similar limitations, while the simplified SIM formula fails to fully account for the complex interaction process, especially for lower energies.

Table 4.1. Theoretical formulas for the intrinsic bremsstrahlung angular distribution, i.e., the shape function (eq. (2.12)), that describe the polar angle of bremsstrahlung emitted in the electric field of a neutral atom. These shape functions were investigated using the EGSnrc Monte Carlo system (Kawrakow *et al.*, 2017).

Theory	Short description
UNI	Uniform spherical distribution commonly assumed in spectrum models
2BS	High-energy PWBA[1] result including screening (Koch and Motz, 1959)
2BN	General PWBA[1] result, assuming a bare nucleus (Koch and Motz, 1959)
KM	2BS formula modified to emulate features of 2BN (Kawrakow *et al.*, 2017)
SIM	The leading term of the 2BN formula (Kawrakow *et al.*, 2017)
KQP	Parametrization by Acosta *et al.* (2002) fitted to numerical PWA[2] results

[1] PWBA — plane-wave Born approximation
[2] PWA — partial wave analysis

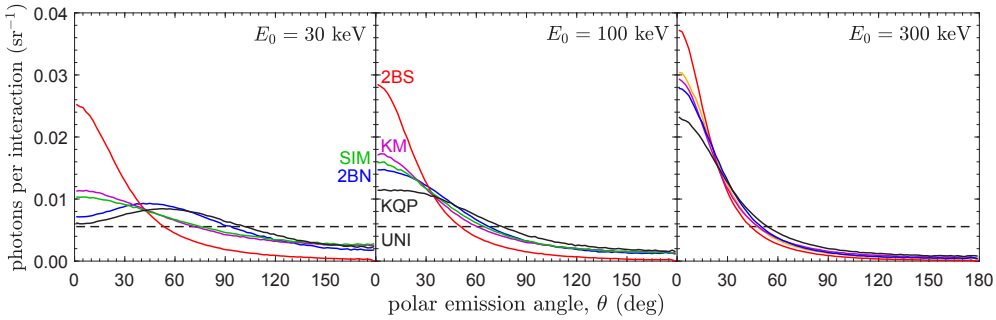

Figure 4.3. Angular distributions of bremsstrahlung emerging from a thin foil tungsten target (<1 incident electron mean free path; 1 nm) bombarded by electrons with kinetic energy E_0. The results were obtained by Monte Carlo calculations (EGSnrc) using different formulas for the intrinsic bremsstrahlung angular distribution (listed in table 4.1). (Adapted from Paper II, Omar *et al.* (2018*c*))

It is important to realize that in thick targets (i.e., typical x-ray tube anodes) the incident electrons undergo multiple elastic scattering, resulting eventually in a diffuse directional distribution. Hence, at sufficient depth, the bremsstrahlung angular distributions predicted using different shape functions converge. Nevertheless, since the onset of diffusion does not occur instantaneously as electrons enter the target, differences can be observed in bremsstrahlung spectra calculated using different shape functions.

Figure 4.4 shows that the simplified SIM intrinsic bremsstrahlung angular distribution is an effective alternative to the more detailed KQP shape function that is based on elaborated calculations in partial-wave expansions. The 2BS Born approximation formula (high-energy result) and the uniform spherical distribution (UNI), however, appear to be less suitable. In Paper II, the UNI shape function was shown to be an inaccurate representation of the intrinsic bremsstrahlung angular distribution, with both the energy distribution and the total amount of energy emitted in a given take-off angle being affected. Bremsstrahlung spectra produced using the UNI shape function deviate from spectra obtained with the KQP shape function by up to 15% in terms of the emitted energy fluence, and 3% in terms of the aluminium half-value layer thickness (HVL). Taking these results into consideration, the SIM and KQP shape functions were implemented in the bremsstrahlung model developed in Paper V (eq. (4.3)). For the sake of completeness, the functional form of these these two shape functions is provided below.

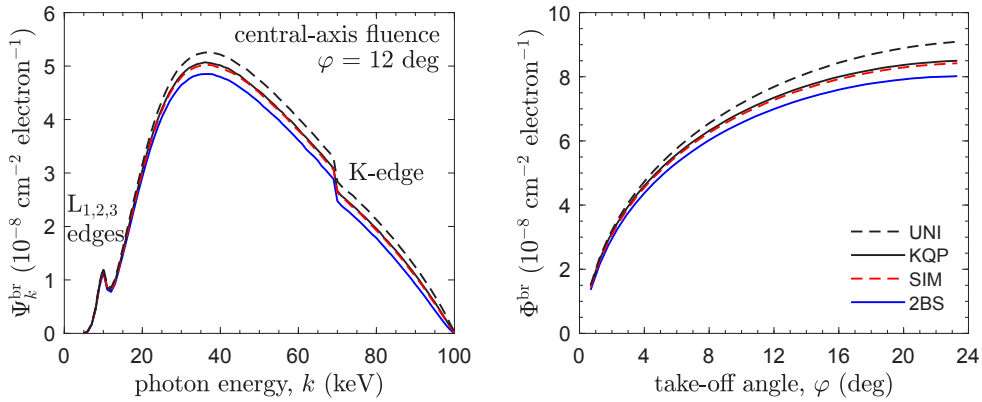

Figure 4.4. Bremsstrahlung emitted from a thick tungsten target tilted 12 deg (i.e., a typical x-ray tube anode angle) per 100 keV incident electron. The left panel shows spectra, i.e., energy fluence differential in energy. The right panel shows the angular distribution, i.e., energy-integrated fluence. The results correspond to Monte Carlo calculations (EGSnrc) with the shape functions listed in table 4.1, except for KM and 2BN, which yield results nearly identical to SIM and KQP. The x-ray beam was filtered by 1 mm beryllium, and the results were scored in air at a distance of 100 cm.

The expression for the KQP shape function is the analytical parametrization derived by Acosta *et al.* (2002), which is the same approach as used in the PENELOPE MC system for the intrinsic bremsstrahlung angular distribution,

$$S^{\rm KQP} = A\frac{3}{16\pi}\left[1+\left(\frac{\cos\theta-\beta'}{1-\beta'\cos\theta}\right)^2\right]\frac{1-\beta'^2}{(1-\beta'\cos\theta)^2} + (1-A)\frac{3}{8\pi}\left[1-\left(\frac{\cos\theta-\beta'}{1-\beta'\cos\theta}\right)^2\right]\frac{1-\beta'^2}{(1-\beta'\cos\theta)^2}, \quad (4.6)$$

with $\beta' = \beta(1+B)$. The parameters A and B depend on (k, Z, E), and are adjusted by least squares fitting to closely approximate the benchmark values produced by Kissel *et al.* (1983), who produced by numerical calculations in partial-wave expansion the most sophisticated results presently available. The parameters were extracted from the PENELOPE materials database, and additional values were determined by natural cubic spline interpolation of $\ln(AZ\beta)$ and $B\beta$. It should be noted that the most recent version of the PENELOPE MC system (version 2018) uses a slightly different form for the fitting parameters, and employs a denser grid of benchmark values, which have been calculated by the computer code developed by Poškus (2018). The code calculates differential cross sections using the same theoretical approach as Kissel *et al.* (1983) for

electron kinetic energies up to 3 MeV. This difference does, however, not noticeably affect x-ray spectra calculated using the bremsstrahlung model developed in this work. The effect generally being less than 0.1% in terms of the aluminium half-value layer thickness for clinically relevant beam qualities.

Since the bremsstrahlung model developed in Paper V accounts for the intrinsic bremsstrahlung angular distribution in detail, it is expected to be more computationally demanding than previous models. In that regard, the SIM shape function may be an interesting alternative to KQP, as it has a simpler functional form that is photon energy-independent,

$$S^{\mathrm{SIM}} = \Delta^{-2} \left(\int \frac{\mathrm{d}\hat{\mathbf{\Omega}}_\gamma}{\Delta^2} \right)^{-1}, \quad \text{with } \Delta = 1 - \beta \cos\theta. \tag{4.7}$$

The effect of using different shape functions in the bremsstrahlung model developed in this work (eq. (4.3)) was evaluated in Paper V. The results are presented in table 4.2, where the beam quality (HVL), intensity (energy fluence), and air kerma free-in-air, of bremsstrahlung spectra emitted with a 12 deg take-off angle (a commonly used anode angle), are compared with narrow-beam MC calculations.

The diffusion approximation combined with a uniform shape function causes the HVL to be overestimated by 1–3%, and the energy fluence and air kerma to be overestimated by 10–30%. Recall that this approach is employed in the popular tungsten spectrum calculation software SpekCalc (Poludniowski *et al.*, 2009). These results are consistent with the observation that the diffusion approximation causes an overestimation of the amount of bremsstrahlung generated at shallow depths in the target (see fig. 4.2). Using a more detailed model for the electron penetration and the intrinsic bremsstrahlung angular distribution (explicit and KQP model), produces results in good agreement with MC; the difference in the HVL, the energy fluence, and air kerma, being generally less than 1%.

Table 4.2 further shows that the average computation time was less than 1 s, except when using the KQP bremsstrahlung shape function for tube voltages exceeding 100 kV (the higher computation time for the molybdenum spectrum was due to the use of a five times denser photon energy sampling). Notice that the simplified SIM shape function can be implemented without substantially compromising the accuracy of the model predictions for tube voltages of 100 kV and above. Indeed, in Paper II, it was shown that the SIM shape function is a good substitute for the more sophisticated KQP shape function for tube voltages exceeding 50 kV. The SIM shape function is therefore a reasonable substitute for KQP, unless a high accuracy is wanted for tube voltages below about 100 kV.

Table 4.2. Relative difference (%) in first and second aluminium half-value layer thickness (HVL), energy fluence (Ψ^{br}), and air kerma free-in-air ($K^{\mathrm{br}}_{\mathrm{air}}$), for spectra predicted using different models for the electron and intrinsic bremsstrahlung angular distributions compared with narrow-beam Monte Carlo calculations (PENELOPE). The results correspond to selected NIST calibration beam qualities (including a 100 cm air gap) for a take-off angle of 12 deg. The average computation time, t (1×2.60 GHz i7-5600U CPU), is provided for comparison. (From Paper V, Omar *et al.* (2020*a*))

Electron model	Brems. model	HVL_1	HVL_2	Ψ^{br}	$K^{\mathrm{br}}_{\mathrm{air}}$	t (s)
Tungsten, NIST M30 (30 kV, 1 mm Be, 0.5 mm Al)						
Diffusion[1]	UNI[3]	2.5	2.9	15	12	0.04
Explicit[2]	UNI[3]	0.5	0.2	1.3	1.1	0.1
Explicit[2]	SIM[4]	−0.3	−0.7	−3.2	−2.4	0.1
Explicit[2]	KQP[5]	0.2	−0.1	−0.7	−0.6	0.3
Tungsten, NIST M100 (100 kV, 3 mm Be, 5.25 mm Al)						
Diffusion	UNI	2.7	3.4	14	11	0.07
Explicit	UNI	1.4	1.7	4.8	3.3	0.1
Explicit	SIM	0.3	0.4	−1.9	−2.2	0.1
Explicit	KQP	0.4	0.5	−1.0	−1.4	0.9
Tungsten, NIST M300 (300 kV, 3 mm Be, 4.25 mm Al, 6.5 mm Sn)						
Diffusion	UNI	1.0	1.0	32	32	0.2
Explicit	UNI	0.6	0.6	17	18	0.2
Explicit	SIM	0.1	0.1	0.3	0.4	0.2
Explicit	KQP	0.1	0.1	0.1	0.1	2.5
Molybdenum, NIST Mo/Mo35 (35 kV, 1 mm Be, 0.032 mm Mo)						
Diffusion	UNI	2.2	3.4	17	11	0.09
Explicit	UNI	0.9	1.3	3.0	1.5	0.2
Explicit	SIM	0.3	0.5	−2.1	−2.4	0.2
Explicit	KQP	0.5	0.8	−0.5	−1.3	1.4

[1] Incident electrons are assumed to instantly attain a diffuse directional distribution.
[2] The electron directional distribution is explicitly accounted for using MC results (eq. (4.5)).
[3] UNI — a spherically uniform intrinsic bremsstrahlung angular distribution.
[4] SIM — a simplified model for the bremsstrahlung angular distribution (eq. (4.7)).
[5] KQP — a detailed model for the bremsstrahlung angular distribution (eq. (4.6)).

4.2 Characteristic x-ray production

In Paper III, an analytical model for the prediction of characteristic x-ray emission from an x-ray tube was developed by considering the depth distribution of x-ray fluorescence in a thick x-ray target. The model was expressed in terms of the notations presented in fig. 4.5, and the definitions of radiative transition probabilities given in section 2.2.2. Using these notations, and assuming that characteristic radiation is emitted isotropically in isotropic media, the differential number of x rays emerging with a discrete energy k (expressed by the Dirac delta distribution, δ), can be formulated as,

$$N^{\mathrm{ch}}_{k,\hat{\mathbf{\Omega}}_{\boldsymbol{\gamma}}}(k,\hat{\mathbf{\Omega}}_{\boldsymbol{\gamma}};Z,E_0) = \sum_{\mathrm{S0,S1}} \delta(k-k_{\mathrm{S0-S1}})\ \upsilon_{\mathrm{S0-S1}}(Z) \times \frac{1}{r_0}\int_0^{\infty}\frac{\mathrm{d}x}{4\pi}\,\phi_{\mathrm{S0}}(x/r_0;Z,E_0)\ f_{\mathrm{ch}}(x,k,\hat{\mathbf{\Omega}}_{\boldsymbol{\gamma}};Z), \quad (4.8)$$

where the summation is over all considered radiative transitions, and ϕ_{S0} is the x-ray fluorescence differential in penetration depth scaled by the electron CSDA range, x/r_0, per electron with kinetic energy E_0 incident upon a target of atomic number Z. The self-filtration of x rays by overlying target material is accounted for by $f_{\mathrm{ch}}(x,k,\hat{\mathbf{\Omega}}_{\boldsymbol{\gamma}};Z)$, which is the transmission of photons with energy k emitted in direction $\hat{\mathbf{\Omega}}_{\boldsymbol{\gamma}}$ from a depth x. The self-filtration can be determined as

$$f_{\mathrm{ch}}(x,k,\hat{\mathbf{\Omega}}_{\boldsymbol{\gamma}};Z) = \exp\Big(-\mu_{\mathrm{wo/co}}(k;Z)\ x\csc\varphi\ \sec\vartheta\Big). \quad (4.9)$$

This equation parallels eq. (4.4) for the self-filtration of bremsstrahlung, with the important difference that Rayleigh (coherent) scattering is excluded from the linear attenuation coefficient, $\mu_{\mathrm{wo/co}}$.

The exclusion of Rayleigh scattering is based on the following rationale. Since the characteristic radiation is emitted isotropically in the target, the resulting angular distribution of Rayleigh scattered x rays is also isotropic, that is, the intrinsic Rayleigh scattering angular distribution is masked by the initial isotropic angular distribution of characteristic x rays. The angular deflection following a Rayleigh interaction has in such case no effect on the number of x rays emerging from the target in a given take-off angle, i.e., the x rays are not attenuated by the process of Rayleigh scattering. This is a useful first-order approximation, but it ignores the fact that the absorption of x rays in the semi-infinite target skews the initial isotropic angular distribution. It was shown in Paper III that by excluding Rayleigh scattering from the linear attenuation coefficient, model predictions of the characteristic x-ray yield can be improved by 1–6%, depending on the incident electron energy considered.

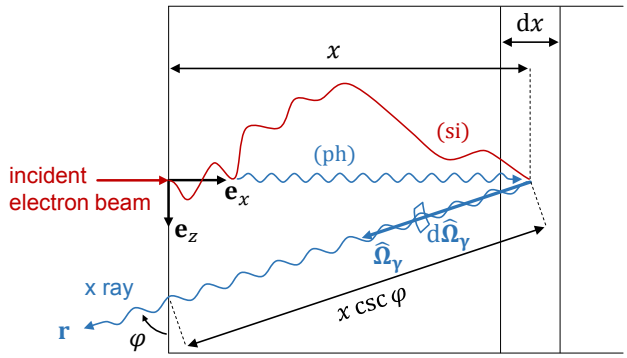

Figure 4.5. Geometry for characteristic x-ray emission from a thick x-ray target. An electron beam penetrates the target, which results in the emission of characteristic energy k in direction $\hat{\mathbf{\Omega}}_\gamma$, following inner-shell ionization caused either by electron impact or photon interaction at depth x (illustrated by the two separate paths labeled (si) and (ph), respectively). The emitted photon exits the target with a take-off angle φ as it propagates toward a point $\mathbf{r}$. (From Paper III, Omar *et al.* (2018*a*))

The described characteristic x-ray model has been implemented in the computational environment MATLAB (available from Omar *et al.* (2018*b*)), with the depth distribution of x-ray fluorescence determined using the PENELOPE MC system. The model was used in Paper III to determine the characteristic x-ray yield and angular distribution. The results are presented in fig. 4.6, along with MC-calculated results.

The figure shows that the model is able to reproduce broad-beam MC results generally to within 2%, which is well within the accuracy of MC calculations compared with experimental results (Bote *et al.*, 2008; Li *et al.*, 2014; Singh *et al.*, 2017). The main reason for the difference between the model predictions and the MC calculations is the Rayleigh scatter contribution from the beryllium window and the air gap. The results shown are relevant for broad-beam applications such as patient dosimetry calculations in medical x-ray imaging. For a narrow-beam geometry, the model is generally within 1% of MC calculations. Narrowly collimated beams are relevant for applications such as imaging with anti-scatter grid, and half-value layer determination. The model is an improvement over previous models mainly in that the self-filtration of characteristic x rays in the x-ray target is more rigorously accounted for, due to the depth distribution of x-ray fluorescence being accounted for in detail using MC-calculated results. This enables more accurate modelling of the angular distribution of x rays emitted from an x-ray tube. It is emphasized that the model predictions were calculated in less than 0.1 seconds (1×2.60 GHz Intel i7-5600U CPU), making the presented model an efficient alternative to comprehensive MC calculations.

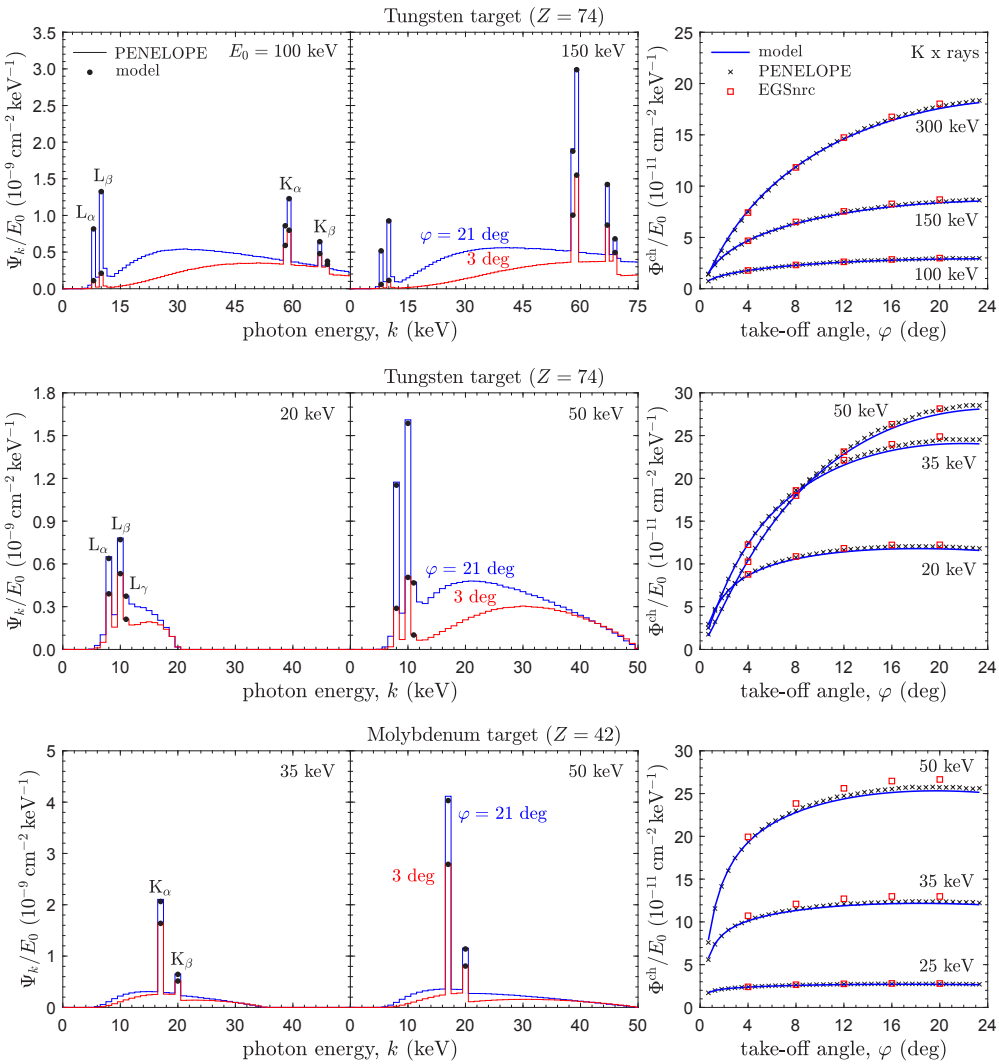

Figure 4.6. X-ray emission per incident electron with kinetic energy E_0. Shown are energy fluence spectra scaled by the incident energy (Ψ_k/E_0; left panels), and the energy-integrated characteristic x-ray fluence as a function of the take-off angle, φ ($\Phi^{\rm ch}/E_0$; right panels). The Monte Carlo (MC) calculations were made for a broad-beam geometry using PENELOPE and EGSnrc, with the x-ray beam filtered by 1 mm beryllium, and the results scored in air at a distance of 100 cm. The model predictions were made using eq. (4.8) with MC-calculated depth distributions of x-ray fluorescence. (From Paper III, Omar *et al.* (2018*a*))

4.3 Validation of the x-ray emission model

The complete x-ray emission model — that is, the bremsstrahlung model described in section 4.1 combined with the characteristic x-ray model described in section 4.2 — has been evaluated in Paper VI. The paper includes comparisons with comprehensive MC calculations, published measured spectra, and models developed by other authors. The different models considered are summarized in table 4.3, which includes both well-established spectrum models as well as more recently published work.

In order to evaluate the performance of the different models, the aluminium HVL has been determined for spectra corresponding to selected NIST calibration beam qualities. The results are presented in table 4.4, where the HVL for the modelled spectra is compared with that obtained by narrow-beam MC simulations. The results correspond to take-off angles of 3, 12, and 21 deg, which covers the range of typically used x-ray tube anode angles and field sizes. In order to get a better sense of the differences between the models, a visual comparison of spectra is provided in fig. 4.7.

Table 4.3. Summary of the x-ray spectrum models used for comparison with the model developed in this thesis. The models are TASMICS (Hernandez and Boone, 2014), MASMICS (Hernandez *et al.*, 2017), IPEM 78 (Cranley *et al.*, 1997), SpekCalc (Poludniowski *et al.*, 2009), SpekPy v1 (Bujila *et al.*, 2020), and xpecgen (Hernández and Fernández, 2016). The electron and intrinsic bremsstrahlung angular distributions used by the different models are listed along with relevant model restrictions. (From Paper VI, Omar *et al.* (2020*b*))

Model	Electron model	Brems. model	Restrictions
Tungsten target models:			
TASMICS	MCNPX[1]	MCNPX[1]	Restricted to 12 deg anode angle
IPEM 78	Thomson-Whiddington[2]	UNI[5]	Anode angle 6–22 deg; energy 30–150 kV
SpekCalc	Diffusion approx.[3]	UNI[5]	No L-lines; cut-off energy 10% of max
SpekPy	Diffusion approx.[3]	UNI[5]	
xpecgen	Explicit[4] (FLUKA)	UNI[5]	No L-lines
This work	Explicit[4] (PENELOPE)	KQP[6]	
Molybdenum target models:			
MASMICS	MCNP6[1]	MCNP6[1]	22.4 deg effective anode angle
IPEM 78	Thomson-Whiddington[2]	UNI[5]	Anode angle 9–23 deg; energy 25–32 kV
This work	Explicit[4] (PENELOPE)	KQP[6]	

[1]TASMICS and MASMICS interpolate spectra calculated using the Monte Carlo system MCNP.
[2]IPEM 78 uses the Thomson-Whiddington law (Whiddington, 1912) for the electron penetration.
[3]Incident electrons are assumed to instantly attain a diffuse directional distribution.
[4]The directional distribution of the electrons is accounted for using Monte Carlo results (eq. (4.5)).
[5]UNI — a spherically uniform intrinsic bremsstrahlung angular distribution.
[6]KQP — a detailed model for the bremsstrahlung angular distribution (eq. (4.6)).

Table 4.4. Relative difference (%) in first and second aluminium half-value layer thickness (HVL), for spectra predicted by the models listed in table 4.3, compared with narrow-beam Monte Carlo (MC) calculations (PENELOPE). The results correspond to selected NIST calibration beam qualities (including a 100 cm air gap) and different take-off angles, φ. (Adapted from Paper VI, Omar *et al.* (2020*b*))

	$\varphi = 3$ deg		$\varphi = 12$ deg		$\varphi = 21$ deg	
model	HVL_1	HVL_2	HVL_1	HVL_2	HVL_1	HVL_2
Tungsten, NIST M30 (30 kV, 1 mm Be, 0.5 mm Al)						
TASMICS	−5.4	−12.6	14.5	5.2	19.7	10.1
IPEM 78	−4.3	−3.4	1.5	1.7	−0.4	−0.9
SpekCalc	8.8	1.0	11.2	3.0	11.9	3.8
SpekPy	−5.8	−0.6	4.0	3.6	6.0	4.9
xpecgen	16.4	7.1	17.6	8.8	18.2	9.5
This work	0.2	−0.1	0.2	−0.1	0.1	−0.2
MC (mm Al)	0.47	0.71	0.39	0.59	0.37	0.56
Tungsten, NIST M50 (50 kV, 1 mm Be, 1.07 mm Al)						
TASMICS	−21.0	−19.5	2.0	0.8	9.4	7.3
IPEM 78	−2.3	−2.9	6.2	4.2	2.3	0.9
SpekCalc	−4.1	−3.1	−2.0	−2.1	−1.2	−1.4
SpekPy	−0.3	1.4	2.1	2.9	3.0	3.9
xpecgen	3.5	3.4	3.9	3.6	4.3	4.3
This work	−0.1	−0.1	0.0	−0.1	0.1	0.1
MC (mm Al)	1.45	2.09	1.12	1.67	1.04	1.57
Tungsten, NIST M100 (100 kV, 3 mm Be, 5.25 mm Al)						
TASMICS	−15.0	−10.4	0.2	−0.3	4.6	2.6
IPEM 78	−0.4	−0.3	4.5	2.6	1.2	0.4
SpekCalc	−0.1	0.5	−0.1	0.7	−0.1	0.8
SpekPy	3.1	2.7	3.4	3.3	3.6	3.6
xpecgen	2.2	1.9	2.0	1.9	1.9	1.9
This work	0.2	0.1	0.4	0.5	0.2	0.3
MC (mm Al)	6.05	7.67	5.13	6.88	4.91	6.70
Molybdenum, NIST Mo/Mo25 (25 kV, 1 mm Be, 0.032 mm Mo)						
MASMICS	−6.8	−6.3	−1.0	−2.5	−0.2	−2.1
IPEM 78	−3.8	−3.7	0.3	−0.9	−1.1	−1.9
This work	−0.2	−0.3	0.0	0.1	−0.3	−0.4
MC (mm Al)	0.31	0.40	0.30	0.38	0.29	0.38

Note that both TASMICS and MASMICS have a fixed take-off angle, and that for IPEM 78 the closest selectable angle has been used.

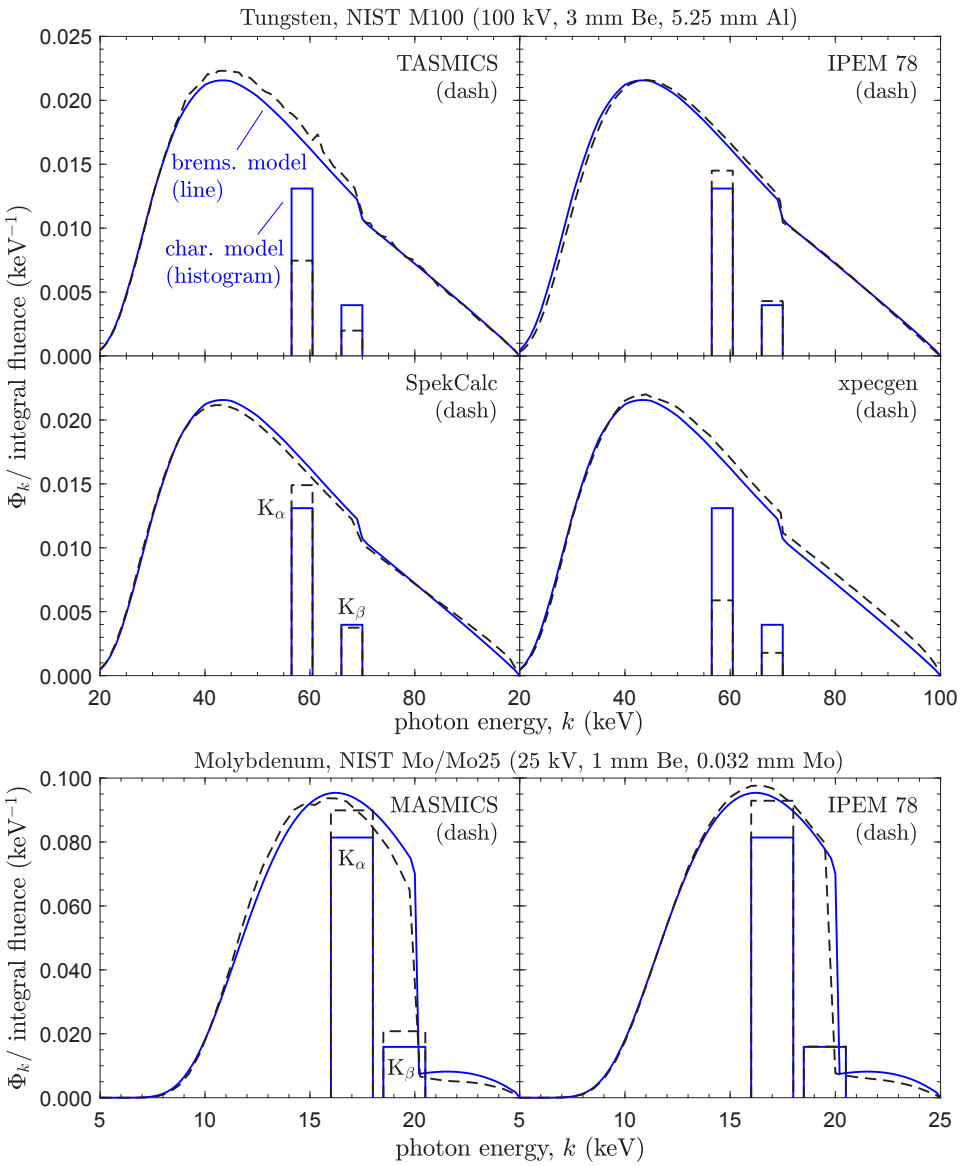

Figure 4.7. X-ray fluence spectra (Φ_k) calculated for the indicated NIST calibration beam qualities assuming a 12 deg take-off angle and an air gap of 100 cm. The model developed in this thesis (solid lines) is in each panel compared with a different analytical spectrum model (specified in table 4.3). Note that the characteristic x-ray peaks have been stripped from the continuous bremsstrahlung spectrum in order to emphasize differences between models in the two distinct spectral components. (From Paper VI, Omar *et al.* (2020*b*))

The model developed in this work performs better than previous models based on theoretical principles (IPEM 78, SpekCalc, SpekPy, and xpecgen), and is generally within 0.5% of MC-calculated results. This can be attributed to the more sophisticated treatment of the physics involved in bremsstrahlung and characteristic x-ray production. Unlike SpekCalc and xpecgen, the present model accounts for x-ray fluorescence following L-shell ionization, which explains the large difference in accuracy observed for the NIST M30 beam quality. Note, however, that for conventional medical x-ray applications, low-energy L x rays are excluded from the spectrum using beam filters, as they contribute little to the image quality while increasing substantially the patient radiation exposure. Nevertheless, accurate modelling of L x-ray peaks is of importance for some low-filtration x-ray beams available at primary standard laboratories such as the National Institute of Standards and Technology (NIST, USA) and the Physikalisch-Technische Bundesanstalt (PTB, Germany).

It should be noted that TASMICS (tungsten) and MASMICS (molybdenum) interpolate MC-calculated x-ray spectra on the central-axis of a broad x-ray beam, assuming an anode angle of 12 and 22.4 deg, respectively. These models are thus valid for a limited range of take-off angles, and they perform worse for take-off angles that deviate from the anode angle, as they do not account for the emission-angle-dependent attenuation of x rays in the target. The TASMICS and MASMICS models are therefore not suitable for modelling the angular distribution of the x-ray emission. The present model, on the other hand, is able to reproduce MC-calculated results to within 1% for a wide range of take-off angles.

Figure 4.7 shows that TASMICS substantially underestimates the amount of tungsten K x rays emitted, and that xpecgen deviates in a similar manner due to the modelled x-ray peak intensity being fitted to TASMICS data (Hernández and Fernández, 2016). In order to better understand these results, model predictions of K x-ray peaks are comped in table 4.5 with published measurements. Again, TASMICS and xpecgen stand out, with the relative amount of K x rays being underestimated by about a factor of two. It is emphasized that the good agreement between SpekPy and MC for the spectrum considered is partly due to the model using an empirical normalization parameter adjusted to match MC-calculated results for a 12 deg take-off angle.

Besides comparing with MC calculations, the model developed in this work has also been compared with spectra measured by Ankerhold (2000) at the German national standards laboratory (PTB). Ankerhold used x-ray tubes with tungsten targets and a high-purity Ge detector to measure pulse height spectra. The measured spectra were unfolded using response matrices determined using the EGS4 MC system (Nelson *et al.*, 1985). The results are presented in figs. 4.8 and 4.9, where the measured characteristic x-ray peaks have been slightly shifted to match the photon energy grid used in the analytical calculations.

Table 4.5. Ratio of K x rays to the total amount of bremsstrahlung and characteristic x rays in a 100 kV spectrum filtered by 1.2 mm Al and 350 cm air, on the central-axis of an x-ray tube with a tungsten target tilted 12 deg (i.e., a 12 deg take-off angle). The results presented correspond to the analytical models specified in table 4.3, narrow-beam Monte Carlo simulations (PENELOPE), and measurements. (Adapted from Paper VI, Omar *et al.* (2020*b*))

Model or data	Method	K_α	K_β	Total
TASMICS	analytical	0.022	0.006	0.028
IPEM 78	analytical	0.044	0.012	0.056
SpekCalc	analytical	0.045	0.013	0.058
SpekPy	analytical	0.035	0.010	0.045
xpecgen	analytical	0.017	0.006	0.023
This work	analytical	0.038	0.011	0.049
PENELOPE	simulated	0.038	0.011	0.049
Bhat *et al.* (1998)	measured	0.038	0.011	0.049
Bhat *et al.* (1999)	measured	0.035	0.012	0.047
Fewell *et al.* (1981)	measured	0.036	0.010	0.046

The results show that in terms of the first and second aluminium HVL, the difference between the modelled and measured x-ray spectra is on average less than 1% (-1.8% to 1.7%). In terms of the mean spectral energy, the difference is on average less than 0.5% (-0.7% to 1.2%). These results demonstrate that the model can be used to reproduce empirical results for a wide range of beam qualities, including the widely used RQA and RQR diagnostic calibration x-ray beam qualities.

In this chapter, an x-ray emission model has been presented and validated. The model has been shown to be an improvement over previous work, especially for low kilovoltage x-ray beams ($\lesssim$ 50 kV). It is also reliable for a wider range of take-off angles, making it suitable for the modelling of off-axis effects such as the (anode) heel effect, which is relevant for certain radiography and mammography applications. Despite the good agreement with measured (narrow-beam) spectra, it is worth pointing out that neither the present nor previous deterministic spectrum models take into-account extra-focal radiation caused by backscattered electrons that reenter the x-ray tube anode; this extra-focal radiation causes the spectrum to be shifted to lower energies. Although approaches for taking into account the extra-focal radiation have been presented in the literature, they are impractical for most applications as they require time-consuming MC simulations of electron transport in the presence of an interelectrode electric field (Ali and Rogers, 2008*a*; van der Heyden *et al.*, 2019). The deterministic model presented in this work is an efficient alternative to comprehensive MC simulations, with calculation times of less than a second.

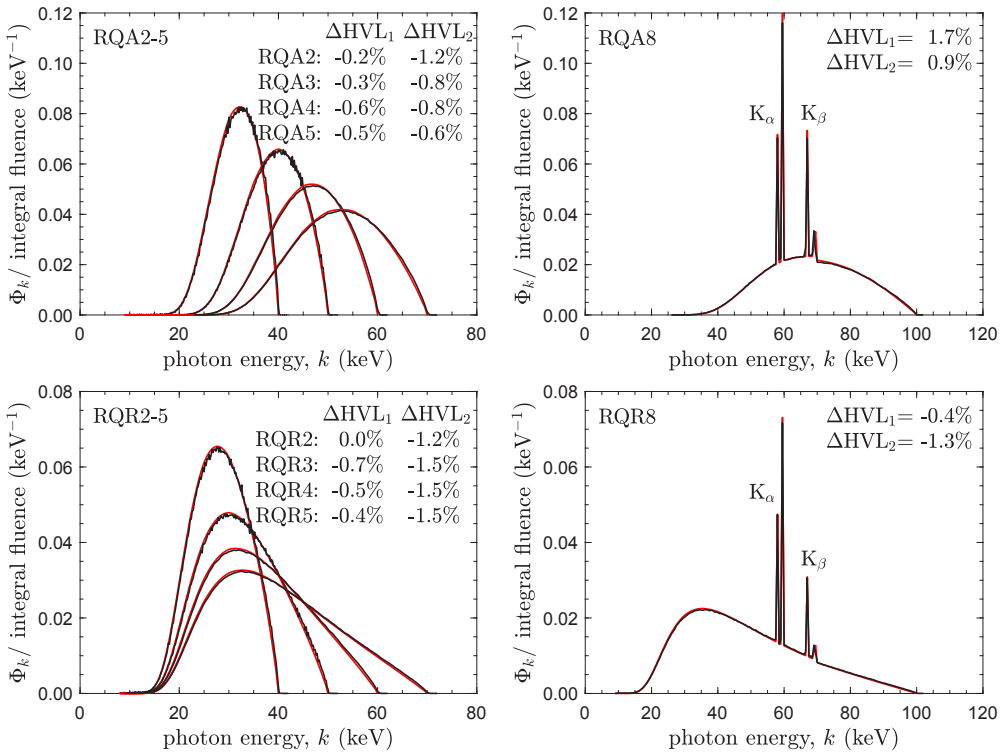

Figure 4.8. X-ray fluence spectra (Φ_k) calculated analytically (red lines) and measured by Ankerhold (2000) (black lines) for selected RQA and RQR diagnostic beam qualities specified by the IEC standard (IEC, 2005). The results correspond to an x-ray tube with a tungsten target tilted 20 deg (i.e., a 20 deg take-off angle), Ankerhold performed the measurements using a narrow-beam geometry and a 100 cm air gap. The figure also shows the the relative difference (%) in first and second aluminium half-value layer thickness between calculated and measured spectra (ΔHVL). (From Paper VI, Omar *et al.* (2020*b*))

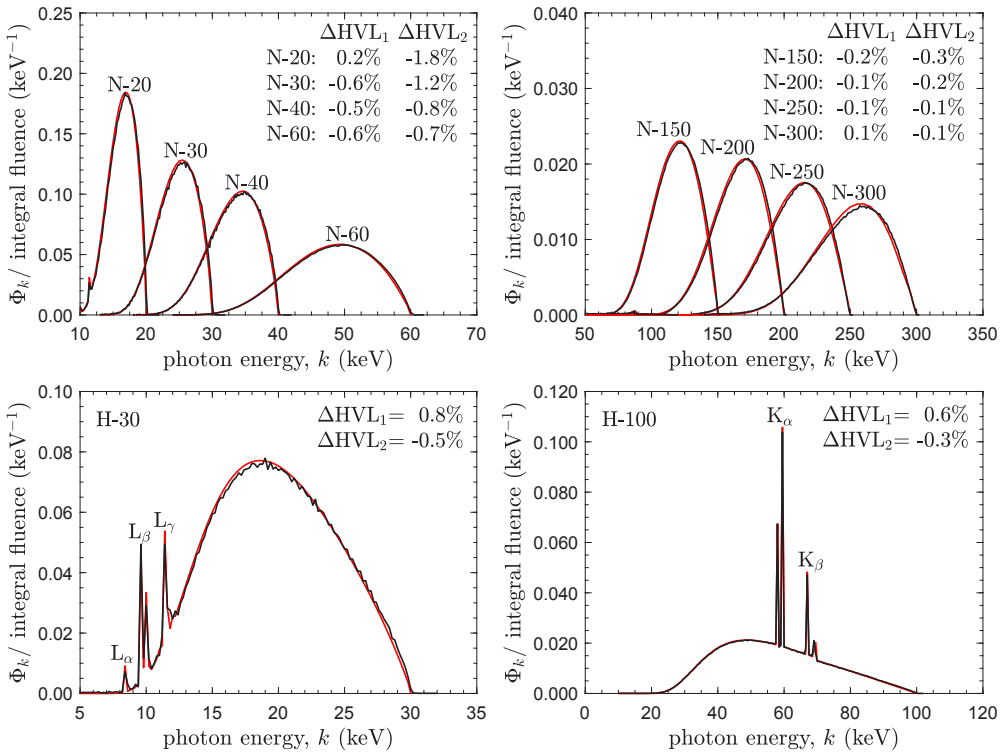

Figure 4.9. X-ray fluence spectra (Φ_k) calculated analytically (red lines) and measured by Ankerhold (2000) (black lines) for selected narrow-spectrum (N-series) and high air-kerma rate (H-series) beam qualities specified by the ISO standard (ISO, 2019). The results correspond to an x-ray tube with a tungsten target tilted 20 deg (i.e., a 20 deg take-off angle), Ankerhold performed the measurements using a narrow-beam geometry and a 100 cm air gap. The figure also shows the the relative difference (%) in first and second aluminium half-value layer thickness between calculated and measured spectra (ΔHVL). (From Paper VI, Omar *et al.* (2020*b*))

Chapter 5

Radiation dosimetry

A framework for systematic patient dose estimation based on dose-related data contained in radiation dose structured reports (RDSR) has been developed in this thesis (chapter 3). The framework can be combined with the x-ray source model outlined in chapter 4, in order to determine organ absorbed doses, effective doses, and entrance surface doses, for medical x-ray examinations. In order to demonstrate how the methods developed in this work can be used in clinical practice and research, they have in this chapter been applied for various dose calculations.

5.1 Organ absorbed dose and effective dose

In Paper I, a prototype implementation of the framework developed in this thesis was demonstrated. The framework was connected to the commercial MC program PCXMC (section 2.3.3), in order to perform patient organ absorbed and effective dose estimations for neuroradiology, adult and paediatric cardiology interventional x-ray examinations. The framework was applied for a total of 150 randomly selected clinical procedures to demonstrate its use for systematic dose estimation in routine clinical practice; the results are summarized in tables 5.1 and 5.2.

The calculation time per patient was 10–20 minutes (2×2.30 GHz Intel Xeon E5-1620 v3 CPUs), depending on the number of x-ray exposures part of the performed x-ray examination. In table 5.1, absorbed doses for the organs of main interest are presented. Notice the distinction between different types of x-ray exposures: radioscopy (serial imaging with a high temporal resolution), radiography (serial imaging with a high contrast resolution), and rotational acquisition (3D volumetric reconstruction). For neurovascular procedures, radiography was the main contributor to the absorbed dose, while for adult cardiovascular procedures the contribution to the

Table 5.1. Mean and standard deviation of organ absorbed doses (mGy) and effective doses (mSv; ICRP 103 (ICRP, 2007*b*)), calculated for 50 neuroradiology, adult and paediatric cardiology interventional x-ray examinations, using the framework developed in this work. The results presented for rotational acquisitions are per rotation. (From Paper I, Omar *et al.* (2016))

	Radioscopy		Radiography		Rotational		Total		
	Mean	σ	Mean	σ	Mean	σ	Mean	σ	Max
Neuroradiology:									
Active bone marrow	1.5	0.2	3.0	0.3	0.4	0.1	4.9	0.5	13.2
Brain	4.3	0.4	27.9	3.3	4.8	0.4	38.5	3.6	116.2
Thyroid	4.7	0.7	3.9	0.5	0.1	0.0	8.7	1.1	35.7
Effective dose	0.9	0.1	1.5	0.2	0.2	0.0	2.6	0.3	8.6
Adult cardiology:									
Active bone marrow	4.3	0.6	3.7	0.4	0.5	0.1	8.1	0.8	25.1
Breasts	1.4	0.2	1.1	0.1	0.1	0.0	2.5	0.3	10.0
Heart	10.4	1.5	9.9	1.2	1.3	0.3	20.5	2.2	76.4
Liver	2.6	0.4	2.6	0.3	0.4	0.2	5.2	0.5	18.0
Lungs	9.8	1.3	9.8	1.1	1.2	0.2	19.7	2.0	78.0
Oesophagus	9.7	1.4	7.8	0.8	1.0	0.3	17.6	1.8	52.9
Stomach	1.1	0.2	1.0	0.1	0.2	0.1	2.1	0.2	9.9
Effective dose	3.0	0.4	2.7	0.3	0.4	0.1	5.7	0.5	18.7
Paediatric cardiology:									
Active bone marrow	1.0	0.2	0.1	0.0	—	—	1.2	0.2	6.6
Breasts	4.1	0.6	0.8	0.2	—	—	5.0	0.7	20.9
Heart	5.1	0.8	1.0	0.2	—	—	6.1	0.9	27.2
Liver	2.1	0.4	0.4	0.1	—	—	2.5	0.4	16.2
Lungs	5.8	0.9	1.0	0.2	—	—	6.9	1.0	29.3
Oesophagus	4.1	0.6	0.7	0.1	—	—	4.8	0.7	18.4
Stomach	1.1	0.2	0.2	0.0	—	—	1.3	0.2	6.4
Effective dose	2.0	0.3	0.3	0.1	—	—	2.3	0.3	8.8

Table 5.2. Air kerma-area product (P_{KA}) to effective dose conversion coefficients, C_E (mSv Gy^{-1} cm^{-2}). (From Paper I, Omar *et al.* (2016))

Procedure	Reference	C_E
Neurovascular	Manninen *et al.* (2012)	0.06–0.07
	NCRP (2009)	0.09
	This work	0.08
Adult cardiology	Compagnone *et al.* (2011)	0.11–0.20
	IAEA (2009)	0.18
	NCRP (2009)	0.12–0.28
	This work	0.22
Paediatric cardiology	Karambatsakidou *et al.* (2009)	(3.7, 1.9, 1.0, 0.6, 0.4)[1]
	This work	(3.2, 2.2, 1.3, 0.8, 0.4)[1]

[1]Corresponds to ages (0–0.5, 0.5–2.5, 2.5–7.5, 7.5–12.5, 12.5–18) years.

absorbed dose was more evenly distributed. This kind of information can be useful for the optimization of clinical practice to reduce the exposure in accordance with the ALARA (As Low As Reasonably Achievable) principle. For paediatric cardiovascular procedures the majority of the absorbed dose was from radioscopy, which was due to a deliberate effort to reduce the exposure of paediatric patients.

In order to compare the results produced in Paper I with results published by other authors, commonly used conversions of air kerma-area product (P_{KA}) to effective dose have been evaluated. Table 5.2 demonstrates a good agreement between the results reported in the literature (based on different methods) and the results produced in this work.

5.1.1 Neuroradiology

In the years following the publication of Paper I, c-arm cone-beam computed tomography (CBCT) imaging (i.e., rotational acquisition) has become increasingly popular. CBCT can be used for pre- and intra-operative diagnosis, followed by minimally invasive intervention, and a post-operative CBCT for verification. CBCT has previously been used for some thrombectomy (ischemic stroke) procedures at Karolinska University Hospital, and the prototype implementation of the framework made it possible to evaluate the radiation doses associated with such procedures. The mean (max) absorbed dose to the brain was estimated to be 110 (520) mGy, with the effective dose being 6 (19) mSv (ICRP 103). The mean absorbed dose to the brain was for CBCT (Philips XperCT Cerebral HD protocol) estimated to be 20 mGy, with the effective dose being 0.7 mSv. Based on these results, it was determined that expanding the clinical use of CBCT to include up to three additional rotational acquisitions could lead to a 35% increase in the total patient dose. This kind of enhanced understanding of the radiation doses involved in the clinic allows for imaging protocols to be optimized and for clinicians to make better informed decisions in their clinical practice.

In addition to the above, intraoperative c-arm CBCT combined with augmented reality spinal surgical navigation has recently been developed at Karolinska University Hospital. The approach makes use of an Allura Clarity Flexmove (Philips Healthcare, Best, the Netherlands) interventional image-guided therapy system. Although there is a clear clinical benefit (improved accuracy of pedicle screw placement; Elmi-Terander *et al.* (2019)), the use of CBCT imaging, instead of the traditional method consisting of c-arm radioscopy image guidance, could lead to patients being exposed to higher radiation doses. Using the prototype implementation of the framework developed in this work, Edström *et al.* (2020) evaluated the organ absorbed and effective doses associated with the described approach. The mean (min–max) absorbed dose to the heart was 30 (0.31–81) mGy, the absorbed dose to the lungs was

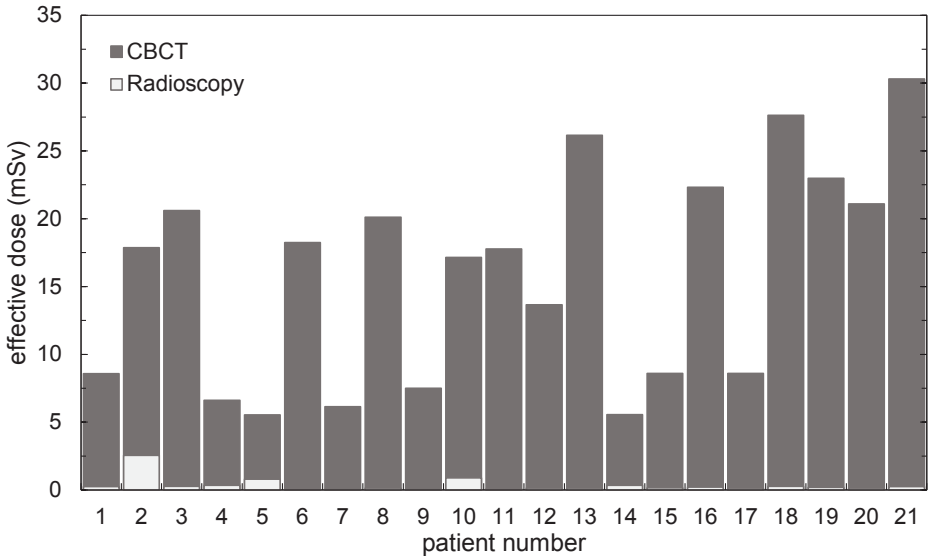

Figure 5.1. Effective doses calculated for spinal surgery procedures performed using a ceiling-mounted c-arm with an integrated augmented reality surgical navigation system. The effective doses were calculated using the framework developed in this thesis (chapter 3), with tissue weighting factors from ICRP 103 (ICRP, 2007*b*). (From Edström *et al.* (2020))

19 (0.22–59) mGy, and the absorbed dose to the stomach was 32 (0.62–75) mGy. The effective doses calculated for the procedures are presented in fig. 5.1.

The average effective dose was 15.8 (5.3–30) mSv, with the variation being both due to the different number of CBCTs per procedure (varied between 2–8) and due to which body part, i.e. organs, were irradiated. For instance, cervical imaging is generally associated with lower radiation doses compared to thoracic or lumbar imaging (Costa *et al.*, 2016). Although the effective doses are indeed higher than the doses delivered using previous clinical methods, i.e., radioscopy imaging, it is worth pointing out that the doses are comparable with that of a single computed tomography (CT) examination. Moreover, the use of intra-operative CBCT imaging renders the need for post-operative CT within 24 hours of the performed procedure (part of the standard care) obsolete; post-operative CTs were not performed for the patients that took part in the study. Considering also that follow-up surgeries may not be needed due to the improved clinical outcome, the cumulative patient radiation dose may be reduced using the novel method. This study demonstrates how the framework can be used to optimize the clinical workflow and enhance the understanding of the different radiation exposures involved in the patient care process.

Recall that the IAEA TRS-457 code of practice (Alm-Carlsson *et al.*, 2007) recommends more accurate dosimetry when the doses delivered may induce tissue reactions. New concerns have recently been raised due to new epidemiological evidence suggesting that some cardio- and neurovascular effects may occur at substantially lower organ absorbed doses than previously considered. Specifically, ICRP (2007*b*) has suggested a dose threshold[1] of 0.5 Gy in absorbed dose to the heart and brain for radiation-induced circulatory diseases (e.g., heart disease and stroke), with the excess relative risk estimated to be about 14% and 9% per unit Gy, respectively (ICRP, 2012).

A study was performed at Karolinska University Hospital to estimate the total cumulative absorbed dose to the brain for patients treated for subarachnoid hemorrhage (Johanna, 2016). The radiation exposure was assessed for both CT and neurointerventional x-ray examinations, with the latter estimated using the framework. It was found that in the study group consisting of 64 patients, 38% of the patients had a cumulative absorbed dose to the brain exceeding the suggested threshold of 0.5 Gy for neurovascular tissue reactions. Moreover, seven patients had a cumulative absorbed dose exceeding 1 Gy and two patients had an absorbed dose of about 2 Gy. Based on this study, it was concluded that although the patient care process is medically motivated, some of the imaging protocols might need to be adjusted to reduce the patient dose (especially for patients below the age of 40), and that magnetic resonance imaging (MRI) may replace some of the CT scans part of the patient care process.

5.1.2 Paediatric cardiology

The exposure of paediatric patients is of particular concern due to children being both more radiosensitive and having a longer remaining life expectancy than adults (ICRP, 2007*a*). Children with congenital heart disease may undergo multiple complex (and thus higher dose) cardiac diagnostic and interventional examinations. In order to gain a better understanding of the doses involved in paediatric interventional cardiology, the radiation dose has been estimated for 202 (108 female, 94 male) patients at Karolinska University Hospital. The results were published in Paper IV, along with a comparison of the method developed in this work (based on detailed DICOM RDSR data) and a simplified method. The simplified method assumed that the entire examination was performed with the heart in the centre of the x-ray field, that the field size was fixed (7×7 cm^2 to 12×12 cm^2, depending on the age of the patient), and that the focus-to-skin distance was fixed at 60 cm.

[1]The concept of *dose threshold* is defined by ICRP (2007*b*) as the estimated (absorbed or equivalent) organ dose for 1% incidence of a tissue reaction in individuals exposed to radiation. For circulatory disease, the threshold refers to a dose delivered that would increase the natural incidence or mortality by 1%.

The paediatric patient doses estimated in Paper IV are presented in table 5.3. The organs of main interest are the ones that received the highest doses: the lungs for 51% of the patients, the heart for 27% of the patients, and the breasts for 21% of the patients. The organ absorbed doses are noticeably higher for older children, which is expected given that their larger size requires a higher x-ray tube voltage and emitted fluence (dose level) to be used in order to generate an adequate x-ray image. It is interesting to note that in terms of the mean dose, the simplified approach is in good agreement with the more detailed approach developed in this work. This is not surprising considering that the simplified assumptions were chosen such that they are representative of the medical procedure. Nonetheless, for individual patients the dose estimation can differ substantially depending on the method used, as is indicated by the large difference in the maximum dose values presented in table 5.3. The difference can be better appreciated in fig. 5.2, which shows the distribution of air kerma-area product to effective dose conversion coefficients (C_E) for different age groups.

It is worth noting that the median conversion coefficients determined using the different approaches agree to within 15% (the difference was found to be statistically insignificant), indicating that the simplified approach can be effectively used for the determination of population doses. For individual patients, the more detailed approach developed in this work may be preferred, as it provides a more realistic account of the clinical patient-to-patient variability. In fact, this variability explains the greater spread in C_E observed in fig. 5.2 for the results obtained using the more detailed approach.

Table 5.3. Mean (max) organ absorbed doses, D_{organ} (mGy), and effective doses, E (mSv; ICRP 103 (ICRP, 2007*b*)), estimated for 202 patients using the framework developed in this thesis (chapter 3), and using the simplified approach described in the text. (Adapted from Paper IV, Karambatsakidou *et al.* (2019))

Age (years)	Method	D_{breast}	D_{heart}	D_{lungs}	D_{marrow}	E
[0–0.5)	This work	5.1 (19)	5.1 (17)	5.4 (18)	0.8 (3.6)	2.1 (7.2)
	Simplified	5.6 (28)	6.6 (32)	7.4 (35)	1.0 (4.7)	2.6 (12)
[0.5–2.5)	This work	4.1 (25)	4.9 (23)	5.0 (18)	0.6 (2.5)	1.7 (6.9)
	Simplified	4.8 (26)	5.0 (22)	5.2 (22)	0.6 (2.8)	1.8 (8.3)
[2.5–7.5)	This work	4.0 (18)	4.4 (19)	5.7 (29)	0.9 (5.0)	1.9 (9.7)
	Simplified	5.5 (45)	5.2 (37)	5.9 (41)	0.7 (4.9)	2.0 (14)
[7.5–12.5)	This work	6.5 (70)	7.2 (43)	8.0 (45)	1.4 (8.0)	2.6 (18)
	Simplified	6.8 (60)	6.0 (45)	7.2 (52)	1.1 (7.7)	2.4 (19)
[12.5–18.0)	This work	8.4 (19)	22 (60)	25 (65)	5.4 (18)	6.6 (15)
	Simplified	12 (27)	18 (81)	26 (130)	4.5 (20)	6.9 (28)

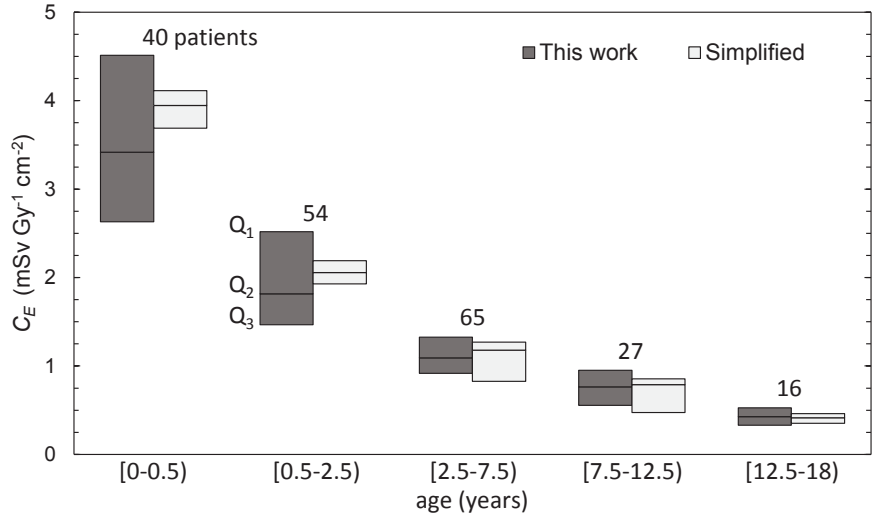

Figure 5.2. Air kerma-area product (P_{KA}) to effective dose conversion coefficients, C_E, for paediatric interventional cardiology procedures. The results are presented as boxplots showing the first (Q_1), second (Q_2), and third (Q_3) quartile value. The results were obtained using the framework developed in this thesis (chapter 3), and using the simplified approach described in the text. (Adapted from Paper IV, Karambatsakidou *et al.* (2019))

The population-averaged organ and effective dose conversion coefficients can be used as input to restrospective epidemiological studies of dose-response for large paediatric cohorts. The organ absorbed doses calculated in Paper IV can also be used to determine the exposure-induced cancer risk, as has been done by Karambatsakidou *et al.* (2020) using the BIER VII risk model (NRC, 2006), which is based on epidemiological studies of Hiroshima and Nagasaki atomic-bomb survivors. They concluded that the average risk of fatal cancer was about 4 in 10,000, with the lungs and breasts contributing the most to the risk. Such studies add to the understanding of the risks involved in paediatric cardiac catheterization, which is useful for both researchers and medical practitioners.

In the above studies, the patient dose calculations were performed using the prototype implementation of the framework described in Paper I, which makes use of the MC program PCXMC. Recall that PCXMC implements the slightly modified stylized (mathematical) phantom models of Cristy and Eckerman (1987) to enable efficient MC dose calculations. However, stylized phantoms are not as realistic as more modern voxelized (tomographic), and hybrid phantom models based on NURBS (Non-Uniform Rational B-Spline) and/or polygon mesh surfaces (Xu, 2014). This

is important to consider, as the main source of error in patient dose calculations is usually the mismatch between the simulated exposure geometry (which includes the patient anatomy) and the actual exposure geometry. Using the stylized phantom models implemented in PCXMC has been shown to introduce substantial errors in dose calculations (exceeding a factor of two), especially for abdominal examinations, due to an incorrect representation of the distribution of fatty tissue (Borrego *et al.*, 2018). However, when averaging over a large population of varying size, the impact of such errors is expected to be reduced. Nevertheless, it is emphasized that the framework for patient dose estimation developed in this work does not rely on the use of a particular method for simulating the radiation transport, or a particular library of phantom models to represent the patient anatomy. The methods described in this thesis can be implemented with different MC code systems and phantom models, depending on the accuracy in dose estimations wanted by the user.

5.2 Entrance surface dose

Determining the patient entrance surface dose, i.e., the absorbed dose to the skin, is relevant for complex interventional radiology examinations that may result in absorbed doses that exceed the threshold for radiation induced skin injury. Recall that the entrance surface dose can be determined as described in section 2.1.2, by multiplying the incident air kerma, $(K_{\mathrm{air}})_{\mathrm{air}}$, with a backscatter factor, B_{air}, and a ratio of mass energy–absorption coefficients, $[\mu_{\mathrm{en}}/\rho]^{\mathrm{p+s}}_{\mathrm{w,air}}$. These quantities depend on the incident x-ray spectrum, which for a given clinical beam quality can be estimated using an x-ray emission model, like the one developed in this thesis (chapter 4). In order to evaluate the performance of different x-ray spectrum models for such calculations, the product of the backscatter factor and the mass energy-absorption coefficient ratio, that is, $D_{\mathrm{w}}/(K_{\mathrm{air}})_{\mathrm{air}}$ (see eq. (2.5)), was determined according to eqs. (2.8) and (2.9), using pre-calculated values of $B_{\mathrm{air}}(k)$ and $[\mu_{\mathrm{en}}(k)/\rho]^{\mathrm{p+s}}_{\mathrm{w,air}}$ published by Benmakhlouf *et al.* (2011). Note that in order to determine the entrance surface dose accurately, the x-ray spectrum model must also be able to reproduce the air kerma free-in-air for different clinical beam qualities. Hence, the energy-fluence weighted mean value of the mass energy-absorption coefficient in air, which coincides with the $(K_{\mathrm{air}})_{\mathrm{air}}$ normalized by the energy fluence, was also determined,

$$\overline{(\mu_{\mathrm{en}}/\rho)}_{\mathrm{air}} = \frac{(K_{\mathrm{air}})_{\mathrm{air}}}{[\Psi]^{\mathrm{p}}_{\mathrm{air}}} = \frac{\int \mathrm{d}k\; k[\Phi_k]^{\mathrm{p}}_{\mathrm{air}}[\mu_{\mathrm{en}}(k)/\rho]_{\mathrm{air}}}{\int \mathrm{d}k\; k[\Phi_k]^{\mathrm{p}}_{\mathrm{air}}}. \tag{5.1}$$

Table 5.4. Relative difference (%) in the ratios of the entrance surface dose to the incident air kerma, $D_{\mathrm{w}}/(K_{\mathrm{air}})_{\mathrm{air}}$, and the mean mass energy absorption coefficient $(\overline{\mu_{\mathrm{en}}/\rho})_{\mathrm{air}}$, calculated using the spectrum models listed in table 4.3, compared with Monte Carlo calculations (PENELOPE). The results correspond to selected NIST calibration beam qualities (including a 100 cm air gap) and take-off angles, φ.

	$\varphi = 3$ deg		$\varphi = 12$ deg		$\varphi = 21$ deg	
model	$D_{\mathrm{w}}/(K_{\mathrm{air}})_{\mathrm{air}}$	$\overline{(\mu_{\mathrm{en}}/\rho)}_{\mathrm{air}}$	$D_{\mathrm{w}}/(K_{\mathrm{air}})_{\mathrm{air}}$	$\overline{(\mu_{\mathrm{en}}/\rho)}_{\mathrm{air}}$	$D_{\mathrm{w}}/(K_{\mathrm{air}})_{\mathrm{air}}$	$\overline{(\mu_{\mathrm{en}}/\rho)}_{\mathrm{air}}$
Tungsten, NIST M30 (30 kV, 1 mm Be, 0.5 mm Al)						
TASMICS	−0.6	10.9	0.5	−6.8	0.7	−10.6
IPEM 78	−0.3	4.8	0.1	−0.4	−0.1	1.6
SpekCalc	0.3	−3.7	0.3	−5.1	0.4	−5.6
SpekPy	−0.2	1.7	0.2	−3.8	0.3	−5.0
xpecgen	0.7	−9.3	0.7	−10.1	0.7	−10.6
This work	0.0	0.0	0.0	0.1	0.0	0.3
Tungsten, NIST M50 (50 kV, 1 mm Be, 1.07 mm Al)						
TASMICS	−3.0	24.5	0.2	−0.7	1.0	−6.8
IPEM 78	−0.4	3.7	0.6	−3.6	0.1	−0.6
SpekCalc	−0.5	3.1	−0.2	1.7	−0.1	0.7
SpekPy	−0.1	−1.2	0.4	−3.1	0.5	−4.2
xpecgen	0.5	−3.6	0.5	−4.0	0.6	−4.7
This work	0.0	−0.1	0.0	0.1	0.0	−0.1
Tungsten, NIST M100 (100 kV, 3 mm Be, 5.25 mm Al)						
TASMICS	−2.3	12.7	0.0	0.0	0.6	−3.0
IPEM 78	0.0	0.2	0.7	−3.1	0.2	−0.7
SpekCalc	0.0	−0.2	0.0	−0.4	−0.1	−0.4
SpekPy	0.4	−2.5	0.5	−3.0	0.5	−3.1
xpecgen	0.3	−1.8	0.2	−1.8	0.2	−1.7
This work	0.0	−0.2	0.1	−0.4	0.0	−0.3

Note that the TASMICS model has a fixed take-off angle, and IPEM 78 has a limited range of angles. $D_{\mathrm{w}}/(K_{\mathrm{air}})_{\mathrm{air}}$ corresponds to a 20×20 cm^2 x-ray field (Benmakhlouf *et al.*, 2011).

Table 5.4 shows quantities related to the determination of entrance surface dose, calculated using the x-ray spectrum models listed in table 4.3. Note that the values of $B_{\mathrm{air}}(k)$ and $[\mu_{\mathrm{en}}(k)/\rho]^{\mathrm{p+s}}_{\mathrm{w,air}}$ entering into the calculations have been determined by MC calculations, in the centre of a 20×20 cm^2 x-ray field on top of a water phantom (Benmakhlouf *et al.*, 2011). The results presented in the table should thus be viewed as calculations for spectra emitted on the central-axis of an x-ray tube with the anode angle corresponding to the take-off angle. Although the range of take-off angles considered exceeds those relevant for typical clinical applications (especially at the lower end of the range), the results demonstrate differences between the models.

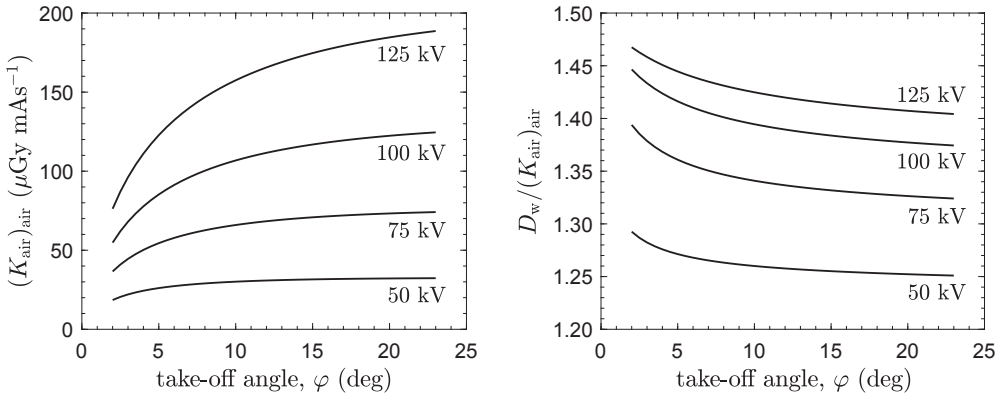

Figure 5.3. Quantities used in the determination of entrance surface dose as a function of the take-off angle for different tube voltages. The left panel shows air kerma free-in-air, $(K_{\mathrm{air}})_{\mathrm{air}}$, at a distance of 100 cm from the x-ray source. The right panel shows ratios of the entrance surface dose to the incident air kerma, $D_{\mathrm{w}}/(K_{\mathrm{air}})_{\mathrm{air}}$, determined using backscatter factors and mass energy-absorption coefficient ratios water to air for a 20×20 cm^2 x-ray field (Benmakhlouf *et al.* (2011)). The results correspond to tungsten spectra filtered by (1 mm Be, 2.5 mm Al, 100 cm air), calculated using the x-ray emission model developed in this thesis.

The values of $D_{\mathrm{w}}/(K_{\mathrm{air}})_{\mathrm{air}}$ estimated using the different spectrum models are in good agreement with MC-calculated results ($\leq 1\%$), except for small take-off angles (3 deg). This is not surprising considering that the backscatter factor and the mass energy-absorption coefficient varies relatively slowly with photon energy, thus making $D_{\mathrm{w}}/(K_{\mathrm{air}})_{\mathrm{air}}$ less sensitive to differences in the spectral shape. In contrast, predictions of $\overline{(\mu_{\mathrm{en}}/\rho)}_{\mathrm{air}}$ show a large variation, due to the mass energy-absorption coefficient in air depending on the photoelectric absorption which drops rapidly with increasing photon energy. It is emphasized that $[\mu_{\mathrm{en}}(k)/\rho]^{\mathrm{p+s}}_{\mathrm{w,air}}$ entering into the calculation of $D_{\mathrm{w}}/(K_{\mathrm{air}})_{\mathrm{air}}$ varies slowly with photon energy because the energy dependence of the photoelectric absorption for air and water varies similarly, thus cancelling each other.

The model developed in this work is an improvement over previous models, especially for the estimation of $\overline{(\mu_{\mathrm{en}}/\rho)}_{\mathrm{air}}$, which is within 0.5% of MC-calculated results. This stems from a more accurate description of both the spectral shape and the fluence emitted for a wide range of x-ray beam qualities and take-off angles. The model can thus be used to estimate the quantities entering into the determination of the entrance surface dose, as shown in fig. 5.3. The model is also able to predict the pronounced (anode) heel effect, and the increase in the backscatter factor for smaller take-off angles and higher tube voltages, as the spectrum is shifted to higher energies.

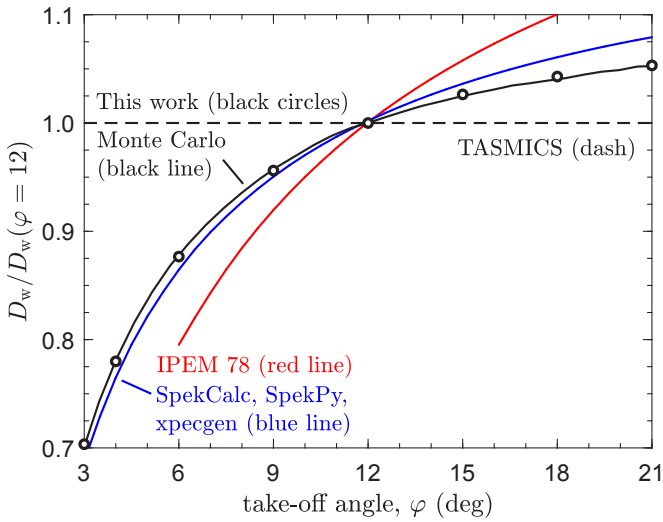

Figure 5.4. Entrance surface dose (D_w) for a 20×20 cm^2 x-ray field as a function of the take-off angle, φ, normalized to 12 deg emission. The entrance surface dose was calculated using different x-ray spectrum models (table 4.3), as well as Monte Carlo calculations (PENELOPE), to determine the incident spectrum, NIST M100 (100 kV, 3 mm Be, 5.25 mm Al, and a 100 cm air gap). The backscatter factors and mass energy-absorption coefficient ratios water to air used in the calculations are from Benmakhlouf *et al.* (2011). Note that SpekCalc, SpekPy, and xpecgen are represented by a single line due to the close similarity of the results.

The patient entrance surface dose is in practice estimated by multiplying $D_w/(K_{air})_{air}$ with a measured or calculated incident air kerma (i.e, the air kerma on the central-axis). In order to determine the absorbed dose to the skin over the entire part of the body exposed by an x-ray beam, a spectrum model can be used to predict the variation in $(K_{air})_{air}$ away from the central-axis. Figure 5.4 shows the entrance surface dose as a function of the take-off angle (normalized to 12 deg emission), calculated for a 20×20 cm^2 x-ray field using different spectrum models. In order to understand the results, recall that the TASMICS model provides the spectrum for a fixed 12 deg take-off angle, and that IPEM 78 uses the Thomson-Whiddington law (Whiddington, 1912) in a way that ignores the effects of electron backscatter and straggling in the target (the models are summarized in table 4.3). SpekCalc, SpekPy, and xpecgen account for these effects, which is why they perform better (within 3% of MC-calculated results). The model developed in this thesis shows additional improvement, and agrees with MC simulations to within 0.5%. This improvement stems from a more detailed account of the electron and intrinsic bremsstrahlung angular distributions.

Chapter 6

Conclusions

The aim of this thesis was to develop methods for radiation dose and x-ray beam modelling that address the challenge of systematic patient dose assessment in medical imaging. Recall that in order to determine the patient dose for a medical x-ray examination, the following aspects of the radiation exposure should be considered:

- The energy and angular distribution of the x-rays emitted from the x-ray tube
- The x-ray exposure geometry and the patient anatomy
- The energy deposited in tissue and organs by the incident x rays

The above points have been the focus of this thesis, which has led to the development of an analytical x-ray emission model, and a framework for estimation of organ absorbed doses in diagnostic and interventional radiology.

The limitations of current x-ray emission models have been investigated using theoretical analysis combined with numerical MC simulations of the depth, energy, and angular distribution of bremsstrahlung and characteristic x rays produced in an x-ray target (i.e., the x-ray tube anode). Based on that, a deterministic x-ray source model was developed that in detail accounts for the electron and intrinsic bremsstrahlung angular distributions. The model is an improvement over previous models developed from theoretical principles in that it provides a more accurate account of the number of x rays emitted in a given direction (i.e., the angular distribution), as well as more accurate predictions of the x-ray energy distribution. It is thus suitable for predictions of both central- and off-axis spectra, as well as off-axis effects such as the (anode) heel effect.

It is worth emphasizing that the model is highly efficient, with calculation times generally a fraction of a second, making it a practical alternative to comprehensive MC simulations. The model is therefore useful for various applications besides medical

imaging, such as, x-ray crystallography, electron-probe microanalysis, security and industrial inspection, as well as low and medium (orthovoltage) energy radiotherapy. The theoretical details of the model have been communicated in several of the papers included in the thesis, but perhaps more importantly, it has been made freely available (under the permissive MIT license) for users of MATLAB (Omar *et al.*, 2020*c*) and Python[1].

The framework for estimation of organ absorbed doses developed in this work makes use of standardized DICOM radiation dose structured reports (RDSR). These reports contain detailed information about the physical context of each x-ray exposure part of a performed x-ray examination. As such, there is no need for additional input from clinical measurements or proprietary access to system-specific exposure data. The approach is therefore general and allows for both systematic and fully automatic patient dose estimation, something that has traditionally not been possible.

The framework includes a novel method for reconstructing the patient-beam alignment based on DICOM RDSR data. The main advantages of the approach is that it is patient-specific, and requires no user input or additional handling of the patient, such as application of fiducial markers. Combining the framework with an x-ray source model (such as the one developed in this work), and an application that converts incident x-ray fluence into organ absorbed dose (e.g., MC), addresses all three aspects of patient dose assessment mentioned in the opening of this chapter. A prototype implementation of the framework has been demonstrated in this thesis for a few selected clinical cases. Such calculations can be used to better understand the patient radiation exposure and the associated risks, which is invaluable for optimization of clinical methods and protocols, and serves to ensure the safe use of radiation in medicine.

[1] SpekPy v2 **URL:** *https://bitbucket.org/spekpy/*

Acknowledgements

First and foremost, I would like to thank my supervisors for continuously supporting and guiding me throughout my studies. This thesis would not have been possible without the invaluable insights and knowledge of my main supervisor, Gavin Poludniowski. You have inspired me to look deep into details, as you have challenged me to understand everything better. I am grateful to my co-supervisor Pedro Andreo for all the things I have learned. Your vast knowledge of the field, combined with a passion for the science, has motivated me to strive for excellence. I am indebted to my co-supervisor Annette Fransson for providing me with the opportunity to pursue this research, and for encouraging me to translate theory into useful practical applications.

I am grateful to my colleagues at Karolinska University Hospital, whose support has allowed me to complete this thesis. In particular, I would like to thank Robert Bujila and Robert Vorbau for being good friends and talented physicists with whom I have had many fruitful discussions. Thank you Angeliki Karambatsakidou for being a great colleague and collaborator in this research. I would also like to thank Hamza Benmakhlouf, Maria Marteinsdottir, and Patrik Nowik, for your friendship and collaboration.

Last but not least, I would like to thank my family for encouraging me to study physics, and for always supporting me.

References

Acosta E, Llovet X and Salvat F 2002 Monte Carlo simulation of bremsstrahlung emission by electrons *Appl. Phys. Lett.* **80**(17), 3228–3230.

Ali E S M and Rogers D W O 2008*a* Quantifying the effect of off-focal radiation on the output of kilovoltage x-ray systems *Med. Phys.* **35**(9), 4149–4160.

Ali E S and Rogers D W 2008*b* Benchmarking EGSnrc in the kilovoltage energy range against experimental measurements of charged particle backscatter coefficients *Phys. Med. Biol.* **53**(6), 1527–1543.

Alm-Carlsson G, Dance D R, DeWerd L, Kramer H M, Ng K H, Pernicka F and Ortiz-Lopez P 2007 *Dosimetry in Diagnostic Radiology: An International Code of Practice* IAEA Technical Reports Series no. 457 International Atomic Energy Agency Vienna, AUT.

Andreo P 1991 Monte Carlo techniques in medical radiation physics *Phys. Med. Biol.* **36**(7), 861.

Andreo P 2019 Data for the dosimetry of low-and medium-energy kV x rays *Phys. Med. Biol.* **64**(20), 205019.

Andreo P, Burns D T, Nahum A E, Seuntjens J and Attix F H 2017 *Fundamentals of ionizing radiation dosimetry* Wiley and Sons.

Andreo P and Nahum A E 2007 Supplementary details on Codes of Practice for absolute dose determination *in* 'Handbook of Radiotherapy Physics – Theory and Practice'. edited by Mayles, P. and Rosenwald, J. C. and Nahum, A. E. (Taylor and Francis, New York and London).

Ankerhold U 2000 *Catalogue of x-ray spectra and their characteristic data—ISO and DIN radiation qualities, therapy and diagnostic radiation qualities, unfiltered x-ray spectra* PTB Report Dos-34 Braunschweig: Physikalisch-Technische Bundesanstalt.

Balter S, Hopewell J W, Miller D L, Wagner L K and Zelefsky M J 2010 Fluoroscopically guided interventional procedures: a review of radiation effects on patients' skin and hair *Radiology* **254**(2), 326–341.

Benmakhlouf H, Bouchard H, Fransson A and Andreo P 2011 Backscatter factors and mass energy-absorption coefficient ratios for diagnostic radiology dosimetry *Phys. Med. Biol.* **56**(22), 7179–7204.

Benmakhlouf H, Fransson A and Andreo P 2012 Influence of phantom thickness and material on the backscatter factors for diagnostic x-ray beam dosimetry *Phys. Med. Biol.* **58**(2), 247.

Berger M J, Coursey J S, Zucker M A and Chang J 2005 *ESTAR, PSTAR, and ASTAR: Computer Programs for Calculating Stopping-Power and Range Tables for Electrons, Protons, and Helium Ions* National Institute of Standards and Technology Gaithersburg, MD.
URL: *http://physics.nist.gov/Star*

Berger M J and Hubbell J H 1987 *XCOM: Photon Cross Sections on a Personal Computer* Report NBSIR 87-3597 National Bureau of Standards (now NIST) Gaithersburg, MD.

Bethe H A and Ashkin J 1953 *in* E Segré, ed., 'Experimental Nuclear Physics' Vol. 1 Wiley New York pp. 166–357.

Bethe H and Heitler W 1934 On the stopping of fast particles and on the creation of positive electrons *Proc. R. Soc. A* **146**(856), 83–112.

Bhat M, Pattison J, Bibbo G and Caon M 1998 Diagnostic x-ray spectra: A comparison of spectra generated by different computational methods with a measured spectrum *Med. Phys.* **25**(1), 114–120.

Bhat M, Pattison J, Bibbo G and Caon M 1999 Off-axis x-ray spectra: a comparison of Monte Carlo simulated and computed x-ray spectra with measured spectra *Med. Phys.* **26**(2), 303–309.

Birch R and Marshall M 1979 Computation of bremsstrahlung x-ray spectra and comparison with spectra measured with a Ge(Li) detector *Phys. Med. Biol.* **24**(3), 505–517.

Boone J M and Seibert J A 1997 An accurate method for computer-generating tungsten anode x-ray spectra from 30 to 140 kv *Med. Phys.* **24**(11), 1661–1670.

Borrego D, Lowe E M, Kitahara C M and Lee C 2018 Assessment of PCXMC for patients with different body size in chest and abdominal x ray examinations: a Monte Carlo simulation study *Phys. Med. Biol.* **63**(6), 065015.

Bote D, Llovet X and Salvat F 2008 Monte Carlo simulation of characteristic x-ray emission from thick samples bombarded by kiloelectronvolt electrons *J. Phys. D: Appl. Phys.* **41**(10), 105304.

Bote D and Salvat F 2008 Calculations of inner-shell ionization by electron impact with the distorted-wave and plane-wave Born approximations *Phys. Rev. A* **77**(4), 042701.

Brusa D, Stutz G, Riveros J A, Fernández-Varea J M and Salvat F 1996 Fast sampling algorithm for the simulation of photon compton scattering *Nucl. Instrum. Methods Phys. Res., Sect. A* **379**(1), 167–175.

Bujila R, Omar A and Poludniowski G 2020 A validation of SpekPy: A software toolkit for modelling X-ray tube spectra *Physica Med.* **75**, 44–54.

Compagnone G, Ortolani P, Domenichelli S, Ovi V, Califano G, Dall'Ara G and Marzocchi A 2011 Effective and equivalent organ doses in patients undergoing coronary angiography and percutaneous coronary intervention *Med. Phys.* **38**(4), 2168–2175.

Costa F, Tosi G, Attuati L, Cardia A, Ortolina A, Grimaldi M, Galbusera F and Fornari M 2016 Radiation exposure in spine surgery using an image-guided system based on intraoperative cone-beam computed tomography: analysis of 107 consecutive cases *J. Neurosurg. Spine* **25**(5), 654–659.

Cranley K, Gilmore B J, Fogarty G W A and Deponds L 1997 Catalogue of diagnostic x-ray spectra and other data IPEM Report No. 78 The Institute of Physics and Engineering in Medicine.

Cristy M and Eckerman K F 1987 *Specific absorbed fractions of energy at various ages from internal photon sources. I. Methods.* Report/TM-8381/V1 Oak Ridge National Laboratory Oak Ridge, TN.

Cullen D E, Hubbell J H and Kissel L 1997 *EPDL97: the Evaluated Photon Data Library, '97 Version* Report UCRL-50400, Vol. 6, Rev. 5 Lawrence Livermore National Laboratory Livermore, CA.

Deslattes R D, Kessler E G, Indelicato P, De Billy L, Lindroth E and Anton J 2003 X-ray transition energies: new approach to a comprehensive evaluation *Rev. Mod. Phys.* **75**(1), 35.

Eckhardt R 1987 Stan Ulam, John von Neumann, and the Monte Carlo method *Los Alamos Science* **15**(131-136), 30.

Edström E, Burström G, Omar A, Nachabe R, Söderman M, Persson O, Gerdhem P and Elmi-Terander A 2020 Augmented reality surgical navigation in spine surgery to minimize staff radiation exposure *Spine* **45**(1), E45–E53.

Elmi-Terander A, Burström G, Nachabe R, Skulason H, Pedersen K, Fagerlund M, Ståhl F, Charalampidis A, Söderman M, Holmin S, Babic D, Jenniskens I, Edström E and Gerdhem P 2019 Pedicle screw placement using augmented reality surgical navigation with intraoperative 3D imaging: a first in-human prospective cohort study *Spine* **44**(7), 517.

European Commission 2015 Medical radiation exposure of the European population, Part 1 Radiation protection report N° 180 Directorate-General for Energy Directorate D - Nuclear Safety & Fuel Cycle Unit D3.

Fewell T R, Shuping R E and Hawkins Jr K R 1981 *Handbook of computed tomography x-ray spectra* Bureau of Radiological Health, U.S. Department of Health and Human Services (FDA) Rockville, MD.

García-Alvarez J A, Fernández-Varea J M, Vanin V R and Maidana N L 2018 Electron–atom bremsstrahlung cross sections in the 20–100 keV energy region: absolute measurements for and comparison with theoretical databases *J. Phys. B: At., Mol. Opt. Phys.* **51**(22), 225003.

Haug E 1975 Bremsstrahlung and pair production in the field of free electrons *Z. Naturforsch.* **30a**, 1099–1113.

Hernandez A M and Boone J M 2014 Tungsten anode spectral model using interpolating cubic splines: Unfiltered x-ray spectra from 20 kv to 640 kv *Med. Phys.* **41**(4).

Hernandez A M, Seibert J A, Nosratieh A and Boone J M 2017 Generation and analysis of clinically relevant breast imaging x-ray spectra *Med. Phys.* **44**(6), 2148–2160.

Hernández G and Fernández F 2016 A model of tungsten anode x-ray spectra *Med. Phys.* **43**(8), 4655.

Hubbell J H and Øverbø I 1979 Relativistic atomic form factors and photon coherent scattering cross sections *J. Phys. Chem. Ref. Data* **8**(1), 69–106.

Hubbell J H, Veigele W J, Briggs E A, Brown R T, Cromer D T and Howerton R J 1975 Atomic form factors, incoherent scattering functions, and photon scattering cross sections *J. Phys. Chem. Ref. Data* **4**, 471–538. Erratum in 6(1977) 615-616.

IAEA 2009 *Establishing Guidance Levels in X Ray Guided Medical Interventional Procedures: A Pilot Study* Safety Reports Series 59 International Atomic Energy Agency Vienna, AUT.

IAEA 2012 *Joint Position Statement on the IAEA Patient Radiation Exposure Tracking* Statement by the European Society of Radiology (ESR), U.S. Food and Drug Administration (FDA), International Atomic Energy Agency (IAEA), International Organization for Medical Physics (IOMP), International Society of Radiographers & Radiological Technologists (ISRRT), World Health Organization (WHO), Conference of Radiation Control Program Directors, USA (CRCPD).

ICRP 1991 *1990 Recommendations of the International Commission on Radiological Protection* ICRP Publication 60, Annals of the ICRP, International Commission on Radiological Protection.

ICRP 1996 *Conversion Coefficients for use in Radiological Protection against External Radiation* ICRP Publication 74, Annals of the ICRP, International Commission on Radiological Protection.

ICRP 2007*a Radiological Protection in Paediatric Diagnostic and Interventional Radiology* ICRP Publication 121, Annals of the ICRP, International Commission on Radiological Protection.

ICRP 2007*b The 2007 Recommendations of the International Commission on Radiological Protection* ICRP Publication 103, Annals of the ICRP, International Commission on Radiological Protection.

ICRP 2012 *Statement on Tissue Reactions / Early and Late Effects of Radiation in Normal Tissues and Organs – Threshold Doses for Tissue Reactions in a Radiation Protection Context* ICRP Publication 118, Annals of the ICRP, International Commission on Radiological Protection.

ICRU 2005 *Patient Dosimetry for X Rays Used in Medical Imaging* ICRU Report 74 International Commission on Radiation Units and Measurements Bethesda, MD.

ICRU 2007 *Elastic Scattering of Electrons and Positrons* ICRU Report 77 International Commission on Radiation Units and Measurements Bethesda, MD.

ICRU 2011 *Fundamental Quantities and Units for Ionizing Radiation* ICRU Report 85 International Commission on Radiation Units and Measurements Bethesda, MD.

IEC 2005 *Medical diagnostic X-ray equipment — Radiation conditions for use in the determination of characteristics* IEC Standard 61267, 2nd ed International Electrotechnical Commission Geneva, CHE.

IEC 2010 Medical electrical equipment – Part 2-43: Particular requirements for the safety of x-ray equipment for interventional procedures *International Electrotechnical Commission 60601 2nd Ed.* .

ISO 2019 *Radiological protection — X and Gamma Reference Radiation for Calibrating Dosemeters and Doserate Meters and for Determining Their Response as a Function of Photon Energy - Part 1: Radiation Characteristics and Production Methods* ISO International Standard 4037-1 2nd edn International Organization for Standardization Geneva, CHE.

Jablonski A, Salvat F, Powell C J and Lee A Y 2016 *NIST electron elastic-scattering cross-section database version 4.0* NIST Standard Reference Database Number 64 National Institute of Standards and Technology Gaithersburg, MD, 20899.
URL: *https://srdata.nist.gov/srd64/*

Johanna J 2016 Subarachnoid hemorrhage: cumulative radiation dose during the patient care process and mapping of vasospasm induced ischemia Master's thesis Karolinska Institutet, CLINTEC, SWE.

Johnson P B, Borrego D, Balter S, Johnson K, Siragusa D and Bolch W E 2011 Skin dose mapping for fluoroscopically guided interventions *Med. Phys.* **38**(10), 5490–5499.

Kagadis G C, Katsanos K, Karnabatidis D, Loudos G, Nikiforidis G C and Hendee W R 2012 Emerging technologies for image guidance and device navigation in interventional radiology *Med. Phys.* **39**(9), 5768–5781.

Kákonyi R, Erdélyi M and Szabó G 2009 Monte carlo analysis of energy dependent anisotropy of bremsstrahlung x-ray spectra *Med. Phys.* **36**(9), 3897–3905.

Karambatsakidou A, Omar A, Fransson A and Poludniowski G 2019 Calculating organ and effective doses in paediatric interventional cardiac radiology based on DICOM structured reports–Is detailed examination data critical to dose estimates? *Physica Med.* **57**, 17–24.

Karambatsakidou A, Sahlgren B, Hansson B, Lidegran M and Fransson A 2009 Effective dose conversion factors in paediatric interventional cardiology *Br. J. Radiol.* **82**(981), 748–755.

Karambatsakidou A, Steiner K, Fransson A and Poludniowski G 2020 Age-specific and gender-specific radiation risks in paediatric angiography and interventional cardiology: conversion coefficients and risk reference values *Br. J. Radiol.* **93**(1110), 20190869.

Kawrakow I, Mainegra-Hing E, Rogers D W O, Tessier F and Walters B R B 2017 *The EGSnrc Code System: Monte Carlo Simulation of Electron and Photon Transport* NRCC Report PIRS-701 National Research Council Canada Ottawa, CAN.

Kerr G D and Eckerman K F 1985 Neutron and photon fluence-to-dose conversion factors for active marrow of the skeleton *in* 'Proceedings of the fifth symposium on neutron dosimetry' Vol. I of *Radiation protection aspects* Munich (Germany).

Khodadadegan Y, Zhang M, Pavlicek W, Paden R G, Chong B, Schueler B A, Fetterly K A, Langer S G and Wu T 2011 Automatic monitoring of localized skin dose with fluoroscopic and interventional procedures *J Digit Imaging* **24**(4), 626–639.

King S D and Spiers F W 1985 Photoelectron enhancement of the absorbed dose from X rays to human bone marrow: experimental and theoretical studies *Br. J. Radiol.* **58**(688), 345–356.

Kissel L, Quarles C A and Pratt R H 1983 Shape functions for atomic-field bremsstrahlung from electrons of kinetic energy 1–500 keV on selected neutral atoms $1 \leq Z \leq 92$ *At. Data Nucl. Data Tables* **28**(3), 381–460.

Koch H W and Motz J W 1959 Bremsstrahlung cross-section formulas and related data *Rev. Mod. Phys.* **31**(4), 920.

Kramers H A 1923 On the theory of x-ray absorption and of the continuous x-ray spectrum *Philosophical Magazine Series 6* **46**(275), 836–871.

Lee C, Lee C, Shah A P and Bolch W E 2006 An assessment of bone marrow and bone endosteum dosimetry methods for photon sources *Phys. Med. Biol.* **51**(21), 5391.

Li X L, Zhao J L, Tian L X, An Z, Zhu J J and Liu M T 2014 Measurements of inner-shell characteristic X-ray yields of thick W, Mo and Zr targets by low-energy electron impact and comparison with Monte Carlo simulations *Nucl. Instrum. Methods Phys. Res., Sect. B* **333**, 106–112.

Liljequist D 1983 A simple calculation of inelastic mean free path and stopping power for 50 eV–50 keV electrons in solids *J. Phys. D: Appl. Phys.* **16**(8), 1567.

Llovet X, Powell C J, Salvat F and Jablonski A 2014 Cross sections for inner-shell ionization by electron impact *J. Phys. Chem. Ref. Data* **43**(1), 013102.

Ma C M, Coffey C W, DeWerd L A, Liu C, Nath R, Seltzer S M and Seuntjens J P 2001 AAPM protocol for 40-300 kV x-ray beam dosimetry in radiotherapy and radiobiology (AAPM TG-61) *Med. Phys.* **28**, 868–893.

Manninen A L, Isokangas J M, Karttunen A, Siniluoto T and Nieminen M T 2012 A comparison of radiation exposure between diagnostic CTA and DSA examinations of cerebral and cervicocerebral vessels. *AJNR Am. J. Neuroradiol.* **33**(11), 2038–2042.

Møller C 1932 Zur theorie des durchgangs schneller elektronen durch materie *Ann. Phys.* **14**, 568–577.

Morin R L, ed. 2019 *Monte Carlo simulation in the radiological sciences* CRC Press.

Motz J W, Olsen H and Koch H W 1964 Electron scattering without atomic or nuclear excitation *Rev. Mod. Phys.* **36**, 881–928.

NCRP 2009 Ionizing radiation exposure of the population of the United States NCRP Report No. 160 Bethesda, MD: National Council on Radiation Protection and Measurements.

Nelson W R, Hirayama H and Rogers D W O 1985 *The EGS4 Code System* Report SLAC 265 Stanford Linear Accelerator Center Standford, CA.

NRC 2006 *Health risks from exposure to low levels of ionizing radiation: BEIR VII phase 2* National Research Council of the National Academies, Washington, DC.

NRC 2012 *Tracking Radiation Exposure from Medical Diagnostic Procedures: Workshop Reports* National Academies Press Washington, DC.

Omar A, Andreo P and Poludniowski G 2018*a* A model for the emission of K and L x rays from an x-ray tube *Nucl. Instrum. Methods Phys. Res. B* **437**, 36–47.

Omar A, Andreo P and Poludniowski G 2018*b Monte Carlo-calculated depth distributions of K and L x-ray fluorescence generated by keV electrons incident upon thick targets made of Au, W, Rh, Mo, Cu, and Cr* Mendeley Data.
URL: *https://data.mendeley.com/datasets/mnr2zx92h3*

Omar A, Andreo P and Poludniowski G 2018*c* Performance of different theories for the angular distribution of bremsstrahlung produced by keV electrons incident upon a target *Radiat. Phys. Chem.* **148**, 73–85.

Omar A, Andreo P and Poludniowski G 2020*a* A model for the energy and angular distribution of x rays emitted from an x-ray tube. Part I. Bremsstrahlung production *Med. Phys.* .

Omar A, Andreo P and Poludniowski G 2020*b* A model for the energy and angular distribution of x rays emitted from an x-ray tube. Part II. Validation of x-ray spectra from 20 to 300 kV *Med. Phys.* .

Omar A, Andreo P and Poludniowski G 2020*c MATLAB implementation of an analytical model for the emission of x rays from an x-ray tube* Mendeley Data.
URL: *https://data.mendeley.com/datasets/hjf5sctyt8*

Omar A, Benmakhlouf H, Marteinsdottir M, Bujila R, Nowik P and Andreo P 2014 Monte Carlo investigation of backscatter factors for skin dose determination in interventional neuro-radiology procedures *in* 'Physics of Medical Imaging' Vol. 9033 (Bellingham: International Society for Optics and Photonics).

Omar A, Bujila R, Fransson A, Andreo P and Poludniowski G 2016 A framework for organ dose estimation in x-ray angiography and interventional radiology based on dose-related data in DICOM structured reports *Phys. Med. Biol.* **61**(8), 3063–3083.

Perkins S T, Cullen D E, Chen M H, Hubbell J H, Rathkopf J A and Scofield J H 1991 *Tables and graphs of atomic subshell and relaxation data derived from the LLNL Evaluated Atomic Data Library (EADL), Z = 1-100* Report UCRL-ID-50400 vol. 30 Lawrence Livermore National Laboratory Livermore, CA.

Poludniowski G G 2007 Calculation of x-ray spectra emerging from an x-ray tube. Part II. X-ray production and filtration in x-ray targets *Med. Phys.* **34**(6), 2175–2186.

Poludniowski G G and Evans P M 2007 Calculation of x-ray spectra emerging from an x-ray tube. Part I. Electron penetration characteristics in x-ray targets *Med. Phys.* **34**(6), 2164–2174.

Poludniowski G, Landry G, DeBlois F, Evans P M and Verhaegen F 2009 SpekCalc: a program to calculate photon spectra from tungsten anode x-ray tubes *Phys. Med. Biol.* **54**(19), N433.

Poškus A 2018 BREMS: A program for calculating spectra and angular distributions of bremsstrahlung at electron energies less than 3 MeV *Comput. Phys. Commun.* **232**, 237–255.

Pratt R H, Tseng H K, Lee C M, Kissel L, MacCallum C and Riley M 1977 Bremsstrahlung energy spectra from electrons of kinetic energy 1 keV $\leq T_1 \leq$ 2000 keV incident on neutral atoms $2 \leq Z \leq 92$ *At. Data Nucl. Data Tables* **20**(2), 175–209.

Raeside D E 1976 Monte Carlo Principles and Applications *Phys. Med. Biol.* **21**, 181–197.

Rana V, Gill K, Rudin S and Bednarek D R 2012 Significance of including field non-uniformities such as the heel effect and beam scatter in the determination of the skin dose distribution during interventional fluoroscopic procedures *in* 'Physics of Medical Imaging (San Diego, Feb. 2012)' Vol. 8313 (Bellingham: International Society for Optics and Photonics).

Rauch P, Lin P J P, Balter S, Fukuda A, Goode A, Hartwell G, LaFrance T, Nickoloff E, Shepard J and Strauss K 2012 Functionality and operation of fluoroscopic automatic brightness control/automatic dose rate control logic in modern cardiovascular and interventional angiography systems: A report of task group 125 radiography/fluoroscopy subcommittee, imaging physics committee, science council *Med. Phys.* **39**(5), 2826–2828.

Ribberfors R 1975 Relationship of the relativistic Compton cross section to the momentum distribution of bound electron states *Phys. Rev. B* **12**(6), 2067.

Rogers D 2006 Fifty years of Monte Carlo simulations for medical physics *Phys. Med. Biol.* **51**(13), R287.

Rogers D W, Faddegon B A, Ding G X, Ma C M, We J and Mackie T R 1995 BEAM: a Monte Carlo code to simulate radiotherapy treatment units *Med. Phys.* **22**(5), 503–524.

Sabbatucci L and Salvat F 2016 Theory and calculation of the atomic photoeffect *Radiat. Phys. Chem.* **121**, 122–140.

Salvat F 2014 *PENELOPE-2014: A Code System for Monte Carlo Simulation of Electron and Photon Transport* Report NEA/NSC/DOC(2014) OECD Nuclear Energy Agency Issy-les-Moulineaux, FRA.

Salvat F, Fernández-Varea J M, Sempau J and Llovet X 2006 Monte Carlo simulation of bremsstrahlung emission by electrons *Radiat. Phys. Chem.* **75**(10), 1201–1219.

Salvat F, Jablonski A and Powell C J 2005 ELSEPA—Dirac partial-wave calculation of elastic scattering of electrons and positrons by atoms, positive ions and molecules *Comput. Phys. Commun.* **165**(2), 157–190.

Scofield J H 1973 *Theoretical photoionization cross sections from 1 to 1500 keV* Report UCRL-51326 Lawrence Livermore National Laboratory Livermore, CA.

Scofield J H 1978 K-and L-shell ionization of atoms by relativistic electrons *Phys. Rev. A* **18**(3), 963.

Sechopoulos I, Ali E S M, Badal A, Badano A, Boone J M, Kyprianou I S, Mainegra-Hing E, McMillan K L, McNitt-Gray M F, Rogers D W O, Samei E and Turner C A 2015 Monte Carlo reference data sets for imaging research: Executive summary of the report of AAPM Research Committee Task Group 195 *Med. Phys.* **42**(10), 5679–5691.

Seco J and Verhaegen F, eds 2013 *Monte Carlo techniques in radiation therapy* CRC press.

Seltzer S M and Berger M J 1985 Bremsstrahlung spectra from electron interactions with screened atomic nuclei and orbital electrons *Nucl. Instrum. Methods Phys. Res., Sect. B* **12**(1), 95–134.

Sempau J, Badal A and Brualla L 2011 A PENELOPE-based system for the automated Monte Carlo simulation of clinacs and voxelized geometries—application to far-from-axis fields *Med. Phys.* **38**(11), 5887–5895.

Servomaa A and Tapiovaara M 1998 Organ dose calculation in medical x ray examinations by the program PCXMC *Radiat. Prot. Dosim.* **80**(1-3), 213–219.

Singh B, Kumar S, Prajapati S, Singh B K, Llovet X and Shanker R 2017 Measurement of angular distributions of K x-ray intensity of Ti and Cu thick targets following impact of 10–25 keV electrons *J. Electron Spectrosc. Relat. Phenom.* **216**, 17–22.

Storm E and Israel H I 1970 Photon cross sections from 1 keV to 100 MeV for elements $Z = 1$ to $Z = 100$ *Nucl. Data Tables* **A7**, 565–681.

Tessier F and Kawrakow I 2008 Calculation of the electron–electron bremsstrahlung cross-section in the field of atomic electrons *Nucl. Instrum. Methods Phys. Res., Sect. B* **266**(4), 625–634.

Theodorakou C and Horrocks J A 2003 A study on radiation doses and irradiated areas in cerebral embolisation *Br. J. Radiol.* **76**(908), 546–552.

Tian L, Zhu J, Liu M and An Z 2009 Bremsstrahlung spectra produced by kilovolt electron impact on thick targets *Nucl. Instrum. Methods Phys. Res., Sect. B* **267**(21), 3495–3499.

Tucker D M, Barnes G T and Chakraborty D P 1991 Semiempirical model for generating tungsten target x-ray spectra *Med. Phys.* **18**(2), 211–218.

UNSCEAR 2008 United Nations Scientific Committee on the Effects of Atomic Radiation: Sources and effects of ionizing radiation Technical report United Nations New York.

van der Heyden B, Fonseca G P, Podesta M, Messner I, Reisz N, Vaniqui A, Deutschmann H, Steininger P and Verhaegen F 2019 Modelling of the focal spot intensity distribution and the off-focal spot radiation in kilovoltage x-ray tubes for imaging *Phys. Med. Biol.* .

Vano E, Gonzalez L, Ten J I, Fernandez J M, Guibelalde E and Macaya C 2001 Skin dose and dose-area product values for interventional cardiology procedures *Br. J. Radiol.* **74**(877), 48–55.

Verhaegen F and Seuntjens J 2003 Monte Carlo modelling of external radiotherapy photon beams *Phys. Med. Biol.* **48**, R107–R164.

Vijayan S, Xiong Z, Guo C, Troville J, Islam N, Rudin S and Bednarek D R 2018 Calculation of forward scatter dose distribution at the skin entrance from the patient table for fluoroscopically guided interventions using a pencil beam convolution kernel *in* 'Physics of Medical Imaging' Vol. 10573 (Bellingham: International Society for Optics and Photonics).

Wagner L K, Fontenla D P, Kimme-Smith C, Rothenberg L N, Shepard J and Boone J M 1992 Recommendations on performance characteristics of diagnostic exposure meters: Report of AAPM Diagnostic X-Ray Imaging Task Group No. 6 *Med. Phys.* **19**(1), 231–241.

Watson P G F and Seuntjens J 2016 Technical Note: Effect of explicit M and N-shell atomic transitions on a low-energy x-ray source *Med. Phys.* **43**(4), 1760–1763.

Wheeler J A and Lamb W E 1939 Influence of atomic electrons on radiation and pair production *Phys. Rev.* **55**, 858–862.

Whiddington R 1912 The transmission of cathode rays through matter *Proc. R. Soc. A* **86**(588), 360–370.

Xu X G 2014 An exponential growth of computational phantom research in radiation protection, imaging, and radiotherapy: a review of the fifty-year history. *Phys. Med. Biol.* **59**(18), R233–R302.